Design, Construction, and Testing of an Experimental Apparatus for Single Optical Pyrometer-Based High-Temperature Differential Thermal Analysis for the Study of Rare Earth Material Properties

Submitted By
Tyler C. Andrews

IN PARTIAL FULFILLMENT OF THE REQUIREMENTS FOR AN UNDERGRADUATE THESIS WITH A

BACHELOR OF SCIENCE IN MECHANICAL ENGINEERING

School of Engineering
Tufts University
Medford, Massachusetts

May 2013

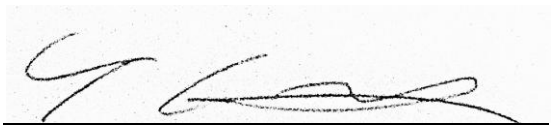

Signature of Author:
Tyler C. Andrews

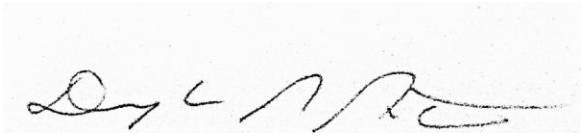

Certified By:
Associate Professor Douglas M. Matson
Department of Mechanical Engineering
Tufts University

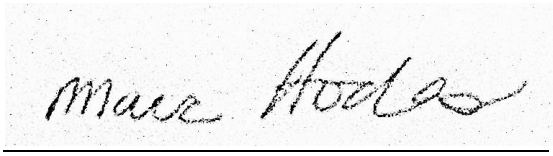

Committee:
Professor Marc Hodes
Department of Mechanical Engineering
Tufts University

Abstract

In this report, a new system for high-temperature, optical-pyrometry-based, differential thermal analysis (DTA) is presented to be used with a previously designed ultra-high temperature induction reactor. Numerical thermal analysis was performed using ANSYS Icepak and COMSOL Multi-physics software. A numerical correlation was established between the heating rate of the reactor and the temperature difference between the reactor and a sample of alumina or silica; this correlation was of the form $dT = A\, e^{b*T}$, where A and b are constants determined by the heating rate. A second correlation was found between the maximum temperature difference, dT_{max}, between samples of silica and alumina and the sample to sample-cup mass ratio, MR, following the function $dT_{max} = 0.0438\, MR^{2.4073}$. A third constant correlation was found between heat of fusion, H_f, and integrated area under a melt-plateau curve, A, as a function $H_f = 0.2983\, A$.

Two physical tests were performed in addition to the thermal analyses described above. In one test, the functionality of a pyrometer-sight designed to focus incoming radiation from four specific areas was found to be effective by showing clear spacing between four readings. In a second test, a thermocouple-based high-temperature differential thermal analysis was performed. Due to significant and inconsistent errors produced by the coupling of induction field and the thermocouple wire, it is recommended that thermocouples not be used in induction-heated apparatuses for high-temperature DTA in the future.

Acknowledgements

The author would like to extend thanks to a number of individuals and organizations, without whose support this project would not have been possible. First, thanks are owed to the author's parents, Tim Andrews and Valerie Cummings whose love and support over the years particularly in all facets of education have shaped him into the person he is. The author would also like to thank Prof. Douglas M. Matson, the author's advisor and mentor throughout the process of researching and writing this thesis, for his guidance and inspiration over the course of the 2012-2013 year. Thanks are also owed to Prof. Marc Hodes, whose aid in thermal modeling and introduction to ANSYS Icepak software were invaluable for the success of this project. In addition to these professors, the author wishes to express gratitude to the entire Tufts University Department of Mechanical Engineering for the opportunity and support. The author would also like to thank Rachel Delucas, Assistant Professor Antoine Alanore, and Professor Don Sadoway of MIT for their help and support. Gratitude is also owed to Jim Hoffman of the Tufts University Machine Shop, without whom this project would not have been possible, and Vincent Miraglia. Finally, thanks are given to fellow graduate and undergraduate students: Brad Nakanishi, Jay Gomes, Alfram Bright, Nate Eckman, Jack Carter, Lisa Lam, Kyle Marks, Olivia Beltrani, Alex Keisling, and the entire Tufts University Cross Country and Track and Field teams for assisting with this project or simply providing support in various ways.

The author would also wish to thank NASA for partial support under grants NNX08AL21G and NNX10AV27G.

Contents

1 Introduction……1
2 Background……4
3 Experimental Apparatus……6
3.1 Engineering Specifications…… 6
3.2 Engineering Design……10
4 Results…….... 25
4.1 Thermal Modeling…… 25
4.2 Experimental Results……46
5 Discussion……..52
5.1 Thermal Modeling…… 52
5.2 Physical Testing……54
5.3 Sources of Error……55
6 Conclusions……60
6.1 Thermal Modeling…… 60
6.2 Physical Testing……61
7 Future Work……...62
8 References……..66
9 Appendix……69

List of Tables

Table 1: Engineering Specifications Required for Design…… 6
Table 2: Engineering Specifications of Custom Pyrometer…….....12
Table 3: Coefficients for Relating Heating Rate to Sample dT……32
Table 4: Difference Coefficients as a Function of Sample:Cup Mass Ratio……43
Table 5: Max dT between Samples as a Function of Mass Ratio……..45
Table 6: Experimental Results of Max Sample dTs for Alumina Melts……51

List of Figures

Figure 1: Rendering of Custom Crusceptode……13
Figure 2: Photo of Custom Crusceptode……14
Figure 3: Photo of Molybdenum Sample Cups…… 15
Figure 4: Biot Number vs. Sample Size for Alumina……17
Figure 5: Biot Number vs. Sample Size for Silica……18
Figure 6: Biot Number vs. Sample Size for Dysprosium…….. 18
Figure 7: Schematic of Sighting Design Logic.....19
Figure 8: Inner Sight Diameter as a Function of Sight Length……..20
Figure 9: Rendering of Final Sight Design……21
Figure 10: Rendering of Sight Gear……...22
Figure 11: Signal Response During Sight Wheel Rotation……... 23
Figure 12: Rendering of Final Sighting Drive-Train Design……24
Figure 13: Photo of Sighting Drive-Train Mounted on Top Cap with Pyro……..24
Figure 14: Screen-shoot of ANSYS Icepak Problem Geometry……... 26
Figure 15: Screen-shoot of COMSOL Problem Geometry……27
Figure 16: Screen-shoot of ANSYS Icepak Transient Setup……28
Figure 17: Screen-shoot of ANSYS Icepak Results at Initial Values……29
Figure 18: Screen-shoot of ANSYS Icepak Results at Transient Values…….. 30
Figure 19: dT Between Alumina and Reactor at 1^{o}C/sec…….. 31
Figure 20: dT Between Silica and Reactor at 1^{o}C/sec……... 31
Figure 21: Coefficients for Relating Heating Rate to Sample dT for Alumina……....33
Figure 22: Coefficients for Relating Heating Rate to Sample dT for Alumina……33
Figure 23: Coefficients for Relating Heating Rate to Sample dT for Silica……..34
Figure 24: Coefficients for Relating Heating Rate to Sample dT for Silica……..34
Figure 25: dT between the Alumina and Reactor Wall for Various HRs……..35
Figure 26: dT between the Silica and Reactor Wall for Various HRs……...36
Figure 27: dT between Samples around Silica Melt-Plateau……37
Figure 28: Scaled dT between Samples around Silica Melt-Plateau……38
Figure 29: Melt-Plateau Integrated Areas as a function of HR…… 39
Figure 30: Standardized Alumina and Silica Heating Curve……40
Figure 31: Close-Up of Standardized Silica Melt Plateau……41
Figure 32: Difference in Temperature between Standardized and 10:1 Ratio……...42
Figure 33: Deviation from Standardized Heating Curve as a Function of Mass Ratio…… 44
Figure 34: dT between samples for Mass Ratio of 10:1…… 45
Figure 35: Max Sample dT during Melt as a Function of Mass Ratio…… 46
Figure 36: Pyrometer Calibration Test Raw Data……47
Figure 37: Overlay of Sample dT during Six Trials of Alumina Melt…….. 51
Figure 38: Close-Up of Alumina Melt Trial #6……57
Appendix Figure 1: Molybdenum Sample-Cup Stamp Design…… 69
Appendix Figure 2: Close-Up of Alumina Melt Trial #1……...70
Appendix Figure 3: Close-Up of Alumina Melt Trial #2……...70
Appendix Figure 4: Close-Up of Alumina Melt Trial #3……...71
Appendix Figure 5: Close-Up of Alumina Melt Trial #4……...71
Appendix Figure 6: Close-Up of Alumina Melt Trial #5……...72
Appendix Figure 7: Close-Up of Alumina Melt Trial #6……...72
Appendix Figure 8: All Raw Thermocouple Data from Test II…… 73

List of Equations

Equation 1: Biot Number Calculation……16
Equation 2: Visible Radiation Response Due to Sight Gear……..22
Equation 3: Polynomial used to Describe Deviation from Standardized Data……..42
Equation 4: Heat Transfer due to Radiation……....56
Equation 5: Heat Transfer due to Conduction…….56

1 Introduction

Differential Thermal Analysis (DTA) is a process by which critical thermal properties of materials can be determined by heating and cooling. In DTA, two samples are heated, with one of the samples, the reference sample, being a material with well-known properties and the other being a material with properties to be determined. Each sample's temperature is measured in a transient state, as the samples are both heated through both samples' melting plateaus. The change in temperature between the two samples is calculated and plotted. When a phase-transformation occurs in one of the samples, the change in temperature between the two samples will increase significantly. This change is due to the melt plateau; as one material's temperature continues to rise, the other maintains its temperature during the melt-plateau until the entire sample has become liquid and the melt is complete [1]. In general, this temperature difference caused by the melt plateau is on the order of 1-10 Kelvin. Typical heating rates used in DTA are 0.1 to 0.2 K/sec [2].

By analyzing the change in temperature of the two samples, two important material properties can be calculated. First, the exact melting temperature of the unknown substance can be determined. This is calculated by determining the temperature at the onset of the spike in the change in temperature plot. Second, the heat of fusion for the phase-transformation can be calculated. This value can be calculated by examining the area under the curve of the spike [3].

In this application, an apparatus has been developed capable of performing DTA on rare earth elements (REEs). REEs are a vital and increasingly important part of our world. REEs are defined as 17 elements of the periodic table, composed of the 15 lanthanides with the addition of yttrium and scandium [4]. REEs are also known as rare earth metals (REMs) due to their metallic qualities, high density and good electrical conductance. Key components of myriad products are composed of these elements, from cigarette lighter flints to color televisions and lasers to high-technology projects like super-conduction. There currently exist no known substitutes for these elements thanks to their specific elemental properties [5].

Despite their importance in current technology, surprisingly little is known with regards to many of the material properties of these REEs [6]. Even less is known about their compounds and mixtures, which have been found to be particularly useful metals. Due to their incredibly high melting temperatures, the technology has not been in existence in the past to properly study REEs and their oxides. The recent advancements in the study of melting of REEs have occurred partially due to their key role in rare earth molten oxide electrolysis, currently being studied at MIT and Tufts University [7 - 9]. These new and recent technological developments, including the Tufts University designed ultra-high temperature induction furnace used in experiments as part of this research have aided significantly in the development of understanding of REEs. Thus, technology currently in development, such as the system described in this report, are invaluable for the advancement of this important field of study.

Currently, there exists no way to perform differential thermal analysis at temperatures high enough to examine melting plateaus of rare earth elements and rare earth oxides. As has been outlined, a lack of knowledge of material properties of rare earth elements and rare earth compounds serve for motivation for development of technology capable of this type of analysis.

The stated goal of this research project was to examine through analytical modeling and physical demonstration the possibility of performing differential thermal analysis at temperatures high enough to melt rare earth elements using the Tufts University ultra-high temperature reactor using a safe and repeatable apparatus.**}** The specific technical goals are outlined in the Engineering Specifications, Table 1 in Section 3.1. To achieve these goals, myriad engineering design decisions and solutions were made which are described in detail in Section 3.2 of this report.

2 Background

In general, DTA is performed using thermocouples. Thermocouples are contact based temperature measurement devices. A contact point between two wires made from different materials is formed at the end of the thermocouple. A voltage is then produced when this point is heated, which can be scaled to correlate the voltage produced with the temperature of the source [10].

However, due to the extremely high melting temperatures of rare earth metals and rare earth oxides, thermocouples were deemed to be unsuitable for DTA in this application. In general, the melting temperatures of the materials being examined are between 2000^{o}C and 2500^{o}C. However, Type C thermocouples, the highest temperature model readily available, are made from tungsten and rhenium and are accurate only up to a range of approximately 2320^{o}C. Thermocouples were deemed to be appropriate only for a calibration test of the DTA apparatus described in this report, discussed in Section 5.2.

Differential thermal analysis has been practiced since the mid-20th century, with early designs presented in papers by Vold in 1949 [11] and Kissinger in 1956 [12] as a study of material properties and reaction kinetics. Since then, enormous progressions have been made in DTA technologies. Significantly more complex experimental apparatuses have been assembled and tested in subjects ranging from materials science [13] to pharmaceutical research [14].

The first optical pyrometers were invented and tested in 1892 by Le Chatelier [15]. Since then, optical pyrometry has expanded into the most popular field of non-contact temperature measurement. As of this writing (April, 2013), optical pyrometry has been used in only limited instances in high temperature DTA. For example, in a paper written by Jaroslave L. Caslavsky, rare-earth compounds were examined using optical thermal differential analysis (ODTA). Using ODTA, the melting point of yttrium aluminum garnet, was reinvestigated and liquid YAG was examined at high temperatures [16].

A second example of ODTA is presented in a 2001 paper by C.D. Cao in which the material properties of Cu-Co alloys were examined. In this paper, an optical pyrometer was used as a non-contact temperature measurement device to perform ODTA in order to determine the miscibility gap of levitated samples [17]. In both this and the previous example, the non-contact nature of pyrometry was found to be vital to the success of the research.

3 Experimental Apparatus

The most significant undertaking in this project was the design, assembly, and testing of an apparatus capable of performing pyrometry-based high-temperature differential thermal analysis using a current design iteration of an induction-heated reactor.

3.1 Engineering Specifications

Due to the complex and innovative nature of this project, it was necessary to consider a variety of engineering specifications. These are presented in Table 1.

Number	Specification	Units	Marginal Value	Optimal Value	Importance (1-3)
1	Temperature Range	^{o}C	1000-2500	500-2800	3
2	Maximum sighting eccentricity	in.	0.0005	0.0001	3
3	Maximum uncertainty in sample temperature difference	^{o}C	5	1	3
4	Sample to sample-cup mass ratio	-	5	10	2
5	Temporal resolution	s^{-1}	50	100	2
6	Total cost	$	<7000	< 5000	2
7	Ease of attachment to current reactor design	n/a	Attachable via new cap	Attachable to current cap	1

Table 1: Engineering specifications required in the development of a high temperature differential thermal analysis apparatus.

First, the most important specification considered was the temperature range which could be accurately read using the pyrometer. It was necessary not only for the pyrometer to be able to read the melting temperature, thus necessitating a very high maximum temperature reading, but also to be able to read a respectively low temperature such that the pyrometer could be calibrated during heating and cooling. A

range of 1000^{o}C to 2500^{o}C was established as a marginal value. This gave ample space for several hundred degrees of calibration before reaching any melting temperatures of materials which would be examined. 2500^{o}C would allow measurement of melting points of most rare-earth oxides, without melting the molybdenum crusceptode. An even wider range of 500^{o}C to 2800^{o}C was established as an optimal value. This would give a greater range for calibration of the pyrometer and allow for the testing of even higher melting-temperature materials. Due to its importance in the research to be conducted with this apparatus, this was given an importance factor of 3 out of 3.

Next, the maximum sighting eccentricity of the apparatus was considered. This was also a vital specification, as the accurate sighting of the pyrometer on the crusceptode was absolutely necessary. Without accurate sighting, the spot of the pyrometer would not be guaranteed to be on the sample and, thus, the temperatures of the samples could be confused with the temperature of the crusceptode, other samples, or heat shield. It was calculated that the absolute maximum eccentricity which could be accepted in the pyrometer sight was 0.0005 inches. This would be considered the marginal value. An optimal value was also established which would provide an even greater margin of safety. This value was determined to be 0.0001 inches. As with temperature measurement, this specification is absolutely critical to the successful function of the apparatus, and thus was given an importance factor of 3 out of 3.

The maximum difference in temperature between the samples was also considered as an engineering specification. Due to the nature of this project, the temperature

resolution of each sample was determined to be less important than the temperature resolution of the difference between the two samples. This value, the difference in temperature between the samples, was determined to be critical to DTA. It is the change in this difference, not in the absolute temperature of each sample, which can be used to calculate melting-temperatures and heat of fusions of the substances being tested. Due to initial thermal modeling, an uncertainty value of +/- 5^{o}C was determined to be the minimal value necessary to perform HTDTA. An optimal value of +/- 1^{o}C was determined to be the optimal value, as this would give an even greater thermal resolution to examine the melt plateau of the material in question. Since this was also a vital aspect of the project, it was given an importance factor of 3 out of 3.

The ratio of the mass of the sample to the mass of the cups was also considered as an important engineering specification. It was deemed important to maximize the ratio of the sample's mass to the mass of the cup holding it. Maximizing this ratio would result in a thermal system which would be dominated by the sample, as opposed to the sample-cup. Since the material properties of the sample, and not the sample-cup, are the desired properties to be measured, it was important to maximize the impact of the sample on the sample/sample-cup thermal system. Based on initial thermal modeling, a marginal sample to sample-cup mass ratio of 5:1 was established. An optimal value of 10:1 would allow the thermal system to be dominated even more strongly by the sample material properties. This ratio was deemed important in the ability to observe the phase-changes of materials, but less important than the aforementioned specifications, and so was given an importance factor for 2 out of 3.

The temporal resolution of the system was considered as well with regards to design of the system. Due to the nature of the design, with one single pyrometer being used to measure temperature of four samples, it was important to have a high temporal resolution in order to best approach a simulation of seeing all four samples at once in real time. Because the system is transient, meaning that the heat of the system is constantly changing, it would be impossible to measure the temperatures of all four samples at the same instant. Nonetheless, it would be a significant aid to feature a high temporal resolution, particularly to observe the melt plateau of each material. A marginal value of 50 samples per second was established, with an optimal value of 100 samples per second. This specification was given an importance rating of 2 out of 3.

As is the nature of any research project, cost was also considered as an important factor of both design and implementation. This factor was considered particularly heavily in regards to the design specifications regarding the pyrometer, as this was found to be the most expensive part of the project by a significant margin. Cost was considered mainly as a limiting factor and so was given an importance rating of 2 out of 3.

Finally, the ease of use and assembly of the entire apparatus was considered, particularly its attachment to the current ultra-high temperature reactor. It was desired to create a system which could be fully integrated with the current reactor set-up. A marginal measure of success was established to be an apparatus which could be attached to the reactor tube via a newly manufactured cap, specifically for this apparatus. An optimal value was described as an apparatus which could be easily

mounted onto the existing reactor cap. Though valuable, these designs were not vital to the success of the apparatus and so were given an importance value of 1 out of 3.

3.2 Engineering Design

Due to the aforementioned engineering specifications, many engineering design solutions were considered, leading to the ultimate design described in this report.

3.2.1 Design Overview

The final apparatus designed in this report is made up of five of important components. First and foremost, a pyrometer is mounted to the top cap of the induction furnace. This pyrometer is sighted on a custom-designed molybdenum crusceptode. Four holes are drilled into the bottom of the crusceptode. In each of these four holes, a molybdenum sample-cup filled with experimental sample is placed, with a second molybdenum cover placed over the sample. The pyrometer is allowed to see only the radiation from the sample cups by means of an optical sighting tube. Finally, a sight-wheel is rotated by a motorized drive train, allowing the pyrometer to focus on just one sample-cup at once.

This design and the decisions made to reach it are described in detail below.

3.2.2 Pyrometer

The first design decision to be made was the selection of the pyrometer to be used in the apparatus. As was outlined the above engineering specifications, there were several important engineering specification which were needed. First, the most important factor being considered, the temperature range, was considered. It was found that the majority of pyrometers found which had a large enough temperature range to fulfill the optimal desired value were significantly above the desired cost of the project. Since a majority of the cost of the project would be accounted for by the pyrometer itself, this factor was strongly considered in the selection of the pyrometer.

With help from Process Sensors, a custom Metis MI16 non-contact infrared-thermometer (pyrometer) with focusable laser-sighting optics was designed and ordered. The custom nature of the design allowed for a temperature range of 500^{o}C to 2600^{o}C, allowing measurement of both the lower-temperature heating process as well as the highest temperature melting points to be examined in the 2400^{o}C to 2600^{o}C range. The adjustable focus and laser sighting were also custom features which would prove very useful in the design and testing phase. Also, a maximum temporal resolution of 100 samples per second was achieved in this design. Thus, the optimal value was achieved, allowing for a careful examination of rapid phase-changes. Full design specifications for the pyrometer used are presented in Table 2.

Model	MI16-0500-2600-1-1-3-13-0-0-0-0-A
Price	$4,835.00
Temperature Range	500°C to 2600°C (932°F to 4712°F)
Spectral Response	1.45um to 1.8um
Emissivity	0.05 to 1.00 Adjustable
Accuracy	±0.4% of measured value in °C or 2°C.
Repeatability	±0.2% of measured values in °C +1°C.
Method of Sighting	Laser
Fiber Optic Cable	Flexible Stainless Steel Sheathed.
Length	8.2 feet (2.5 meters) standard
Miniature Optics	Focus range: 4” to 24” (100mm) to (600mm)
Optics Type	OL12-A0 (miniature)
Spot Size Diameter	0.040” to 0.28” (1mm to 7mm)
Analog Output	4mA to 20 mA linear, 500 Ω max. Load
Response Time t90	1 ms, adjustable up to 10 s
Digital Output	RS 232 (Provides raw signal directly from A/D)
Power Requirement	15 to 30 VDC

Table 2: Engineering specifications for custom pyrometer.

3.2.3 Crusceptode, Sample-Cups, and Samples

A custom crusceptode was designed specifically for this application and this apparatus. It was desired to have store at least two, and up to four, samples in the crusceptode. It was also desired to have these samples be heated almost entirely due to radiation.

Thus, a crusceptode was designed with cylindrical holes in which individual up to four samples could be stored, see Figures 1 and Figure 2.

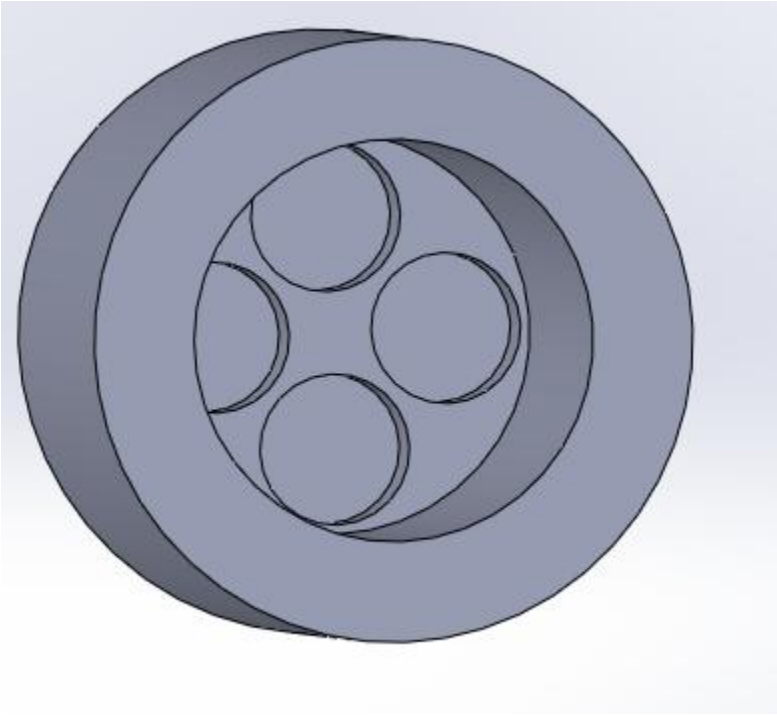

Figure 1: A solid-model rendering of the custom crusceptode, with four sample holes drilled into the bottom. Model designed and rendered using SolidWorks Software

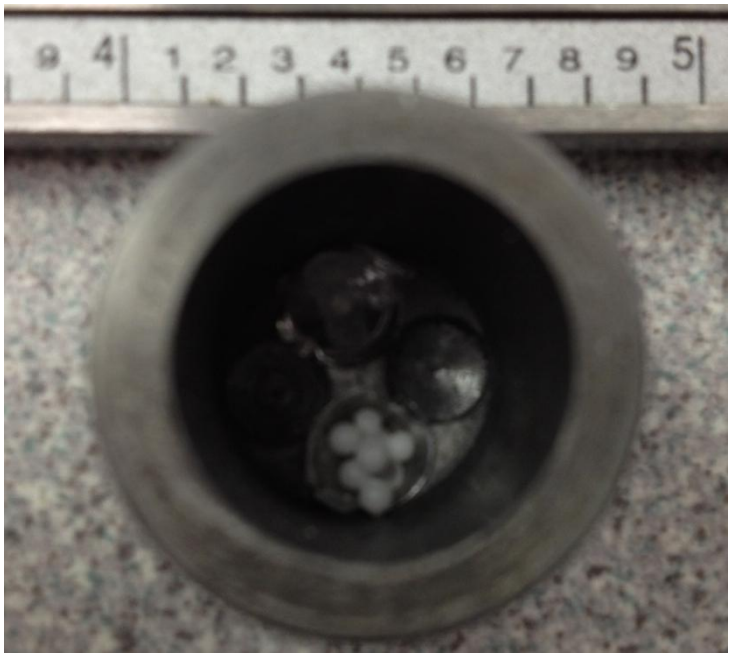

Figure 2: A photo of the custom machined molydbenum crusceptode, with a metric ruler for scale. Two molybednum sample cups can be seen in the North and South crusceptode holes, with the North sample being silica and the South sample alumina.

However, it was decided that the samples could not be heated directly in the crusceptode, as the significant mass of the crusceptode would dominate the thermal system of the sample and crusceptode. It was thus decided to design a specific sample-cup, of very small mass, which could hold the sample in the holes.

Various manufacturers were consulted in an attempt to outsource the manufacturing of the sample-cups. Unfortunately, it was found that all companies consulted were unwilling or unable to provide an appropriate product given the timescale and price-range needed for this project. Too small batch quantities were generally cited as the reason for the inability or unwillingness to produce the cups.

A stamp was designed which could punch a thin metal foil into the desired shape of the cup, as seen in Appendix Figure 1. This stamp was machined and tested with aluminum foil as a proof of concept. The result was the successful product of aluminum foil cups, see Figure 3.

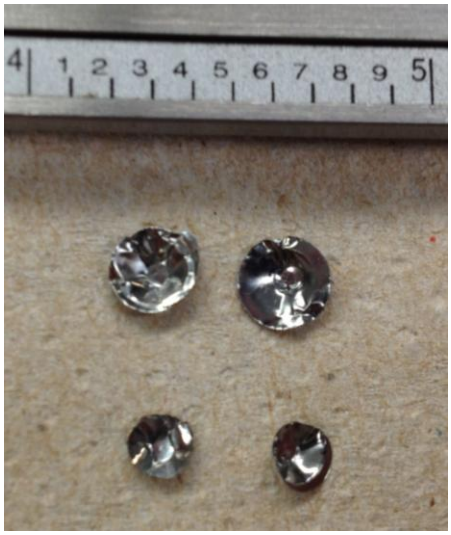

Figure 3: Molybdenum sample cups (above) and sample cup lids (below) next to an English ruler for scale. Sample-cups are filled with samples and covered in sample-cup lids. This allows for a known and predictable emissivity on which to sight the pyrometer.

However, due to its low melting point, aluminum would not be used as the sample-cup. Instead, molybdenum foil was examined. To minimize the mass of the cups, several thin molybdenum foils were tested for feasibility. Four foil thicknesses were tested for feasibility. These foils ranged from 0.015mm to 0.5mm.

It was determined that the thinnest of the foils test, at 0.015mm, would be the lowest mass and most similar to the successful aluminum foil tests. The molybdenum cups

were successful manufactured and were measured to have a mass of 5.52mg +/- 0.03mg. In the current manufacturing process, molybdenum foil is first punched into 5mm discs using a standard hole-punch. These discs are then placed into the female stamp mold where they are pressed by hand with the male mold to press the disc into the desired sample-cup shape.

Finally, the samples themselves were considered. It was desired to have a sample with as large a mass as possible given the physical constraints of the reactor, having to fit inside the samples cups inside the crusceptode. Moreover, it was also necessary to consider the isothermality of the samples. Because the melting points and melting plateaus of the samples are to be examined in DTA, it is important to have the samples as close to perfectly isothermal as possible. With a perfectly isothermal sample, the melt would occur simultaneously at all points in the sample. In DTA, this would be ideal as it would provide the clearest and most accurate representation of the melting point of the sample.

In order to determine the relationship between sample size and isothermality, the sample's Biot number was considered. Biot numbers were calculated according to the equation:

$$Bi = \frac{R_{int}}{R_{ext}} = \frac{h_{rad}\, L}{k}$$

Equation 1: Calculating Biot numbers (Bi) for samples with $h_{rad} = \varepsilon\sigma(T_s^2+T_{surr}^2)(T_s+T_{surr})$, L = sample length, k = sample thermal conductivity, ε= sample emissivity, $\sigma = 5.678 \times 10^8$ W/m^{2}K^4 (the Stefan-Boltzmann Constant) [18]

Biot numbers for the samples were then plotted as a function of L, sample length, to determine the response of Biot number to the physical size of the sample. Four samples were considered: two reference samples (alumina and silica) and one rare-earth sample (Dysprosium). The results can be seen in Figures 4 through 6

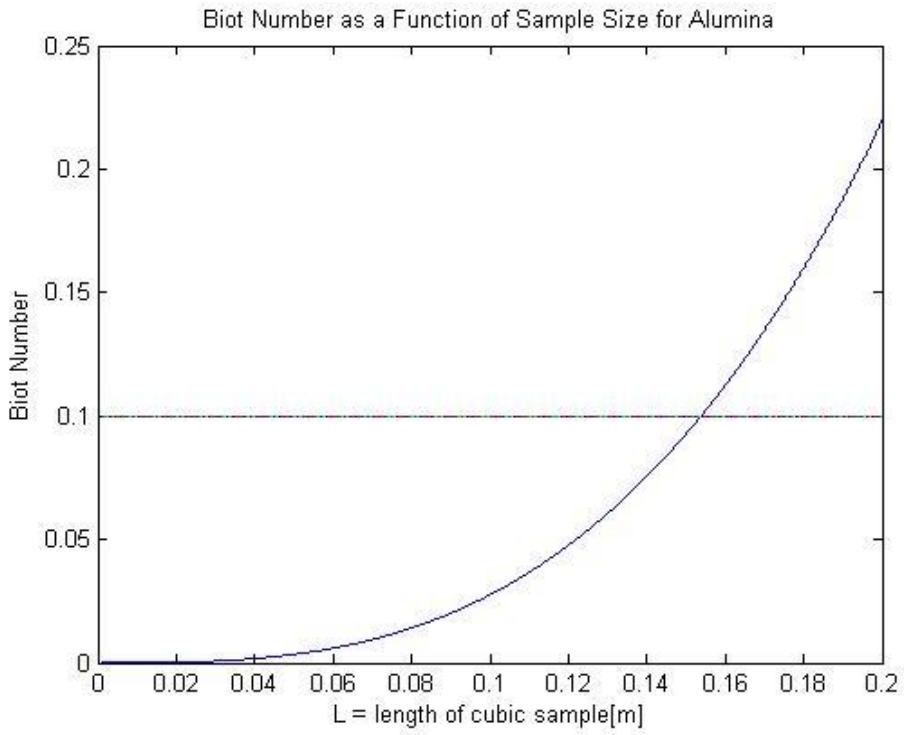

Figure 4: Biot number as a function of sample size for a sample of alumina. Samples with a Biot number of less than 0.1 can be considered isothermal.

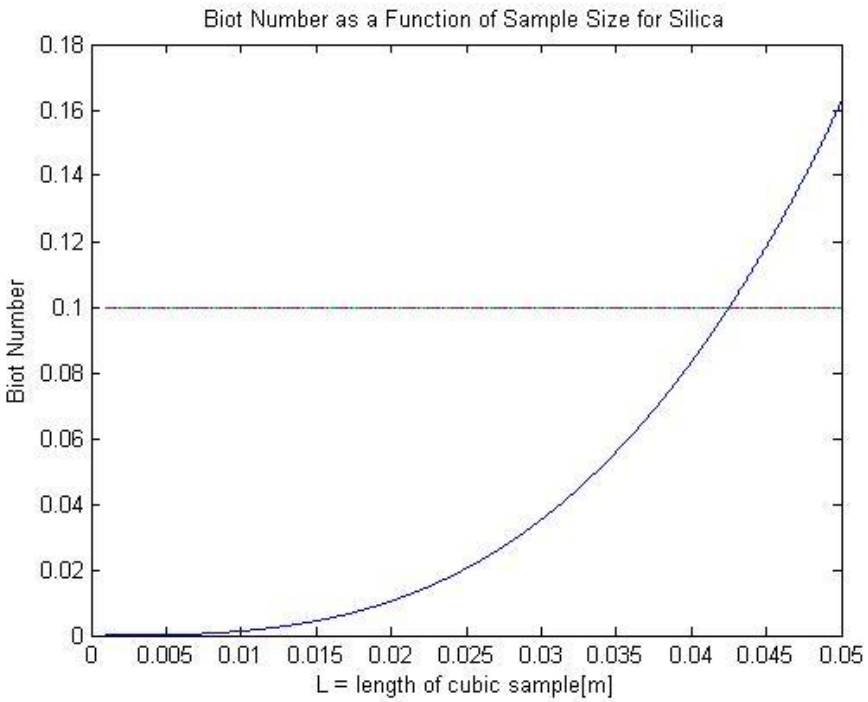

Figure 5: Biot number as a function of sample size for a sample of silica. Samples with a Biot number of less than 0.1 can be considered isothermal.

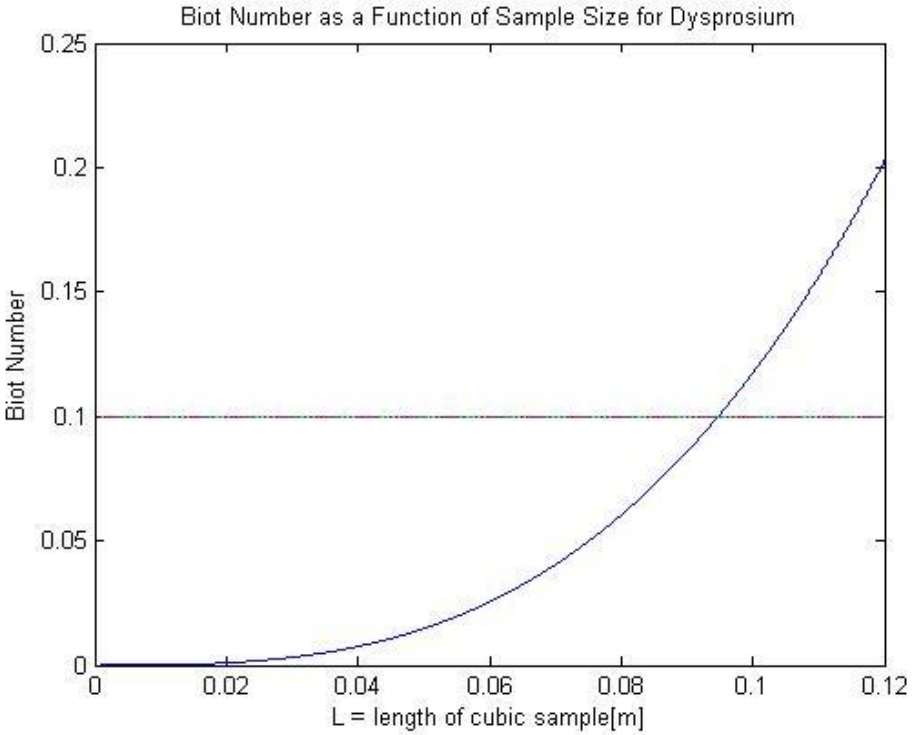

Figure 6: Biot number as a function of sample size for a sample of dysprosium. Samples with a Biot number of less than 0.1 can be considered isothermal [19].

3.2.4 Sighting-Tube and Drive Train

It was necessary to design this apparatus using the single pyrometer outlined above. A challenge was thus presented, in the need to be able to accurately measure the temperatures of multiple samples using only one pyrometer.

In order to accomplish, a sighting apparatus was designed. First, it was desired to create a sighting mechanism which would allow the pyrometer to view only the molybdenum sample-cup tops. In order to accomplish this, a physical sighting scope was designed. Four cylindrical holes were designed to allow only the radiation from each cup to be seen by the pyrometer. As shown in Figure 7, the ability to focus the sight on these very small areas was dependent on the length of the sight and the width of the holes. A sight length of one inch was decided upon to keep the sight from being unwieldy or from bending or buckling. A mounting ring was also designed to mount the pyrometer head over the sighting tube. This entire part was 3D printed to allow for rapid prototyping and testing of the apparatus.

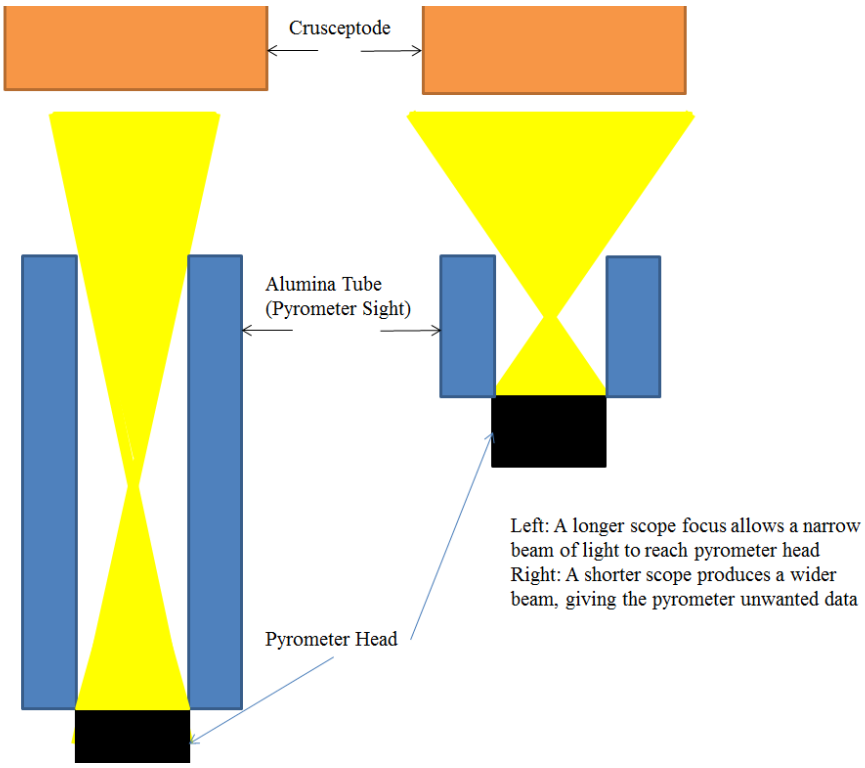

Figure 7: A general schematic showing that a longer pyrometer sight tube blocks out radiation from sources other than the desired radiation from the crusceptode.

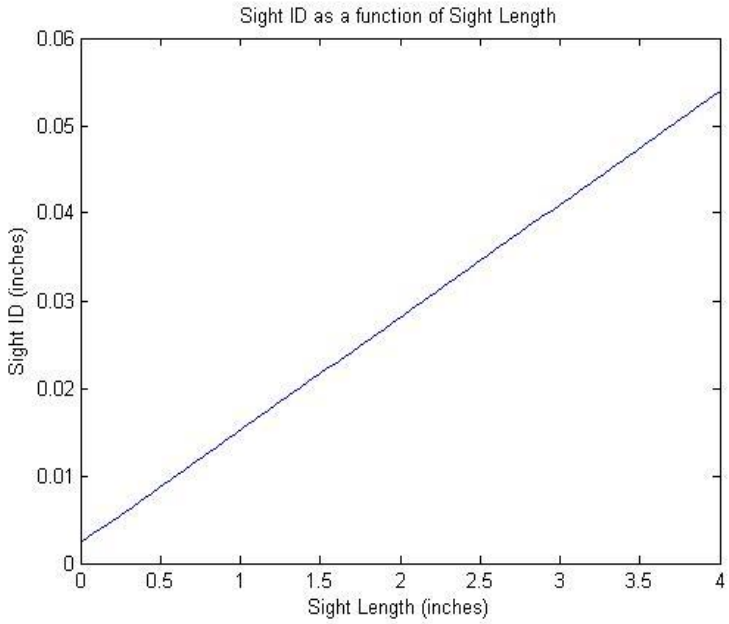

Figure 8: The inner diameter of a sighting hole as a function of length of the sight in order to focus on a spot of light to a radius of 0.00238m at a distance of 0.1143m (4.5 inches).

Do to inaccuracies and low resolution in the 3D printer, a second iteration of this part was designed. In this second iteration, the tubes which penetrated the length of the sighting scope were made wider than necessary. The sighting scope was then covered with two thin caps. The correct sight-hole diameters were cut into these caps, manufactured from laser-cut acrylic, and sanded down to a width of approximately 0.0125". With these two caps, the functionality was equivalent to the original scope design, see Figure 9.

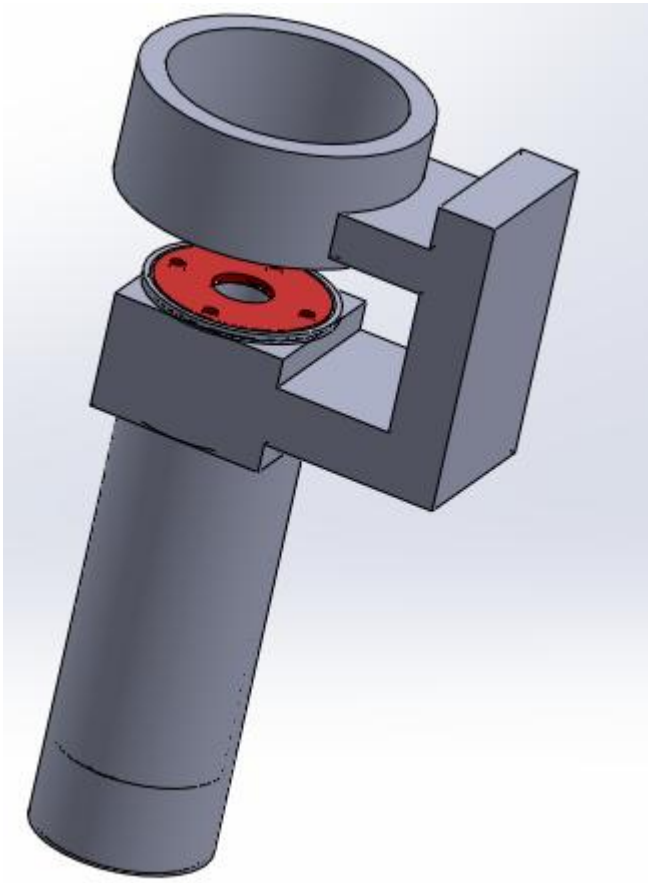

.

Figure 9: A solid-model render of the final design of the sighting tube. The red disc represents the laser-cut piece designed to focus the radiation specifically on the samples.

With the ability to sight the pyrometer on the four sample cups from the top cap of the reactor, a system was needed in order to focus the pyrometer on only one sample at a given time. Thus, a model was designed in which a rotating disc featuring a slit (see Figure 10) was rotated over the scope to allow the viewing of each sample in succession.

Figure 10: A render of the sighting gear used to isolate one sight tube and allow the four sample cups to be measured using one pyrometer.

Due to the shape of the hole, a signal seen by the pyrometer will appear as a sinusoidal approach to a maximal value and a similar sinusoidal decay to 0. This response is due to the function dictating the area of a vertical section of a circle,

$$A = \frac{R^2}{2}(\theta - sin\theta).$$

Equation 2: Calculation of radiation visible to pyrometer, where R = radius of sight inner diameter and θ = angle of rotation across the sight hole [radians]

This response is plotted in Figure 11.

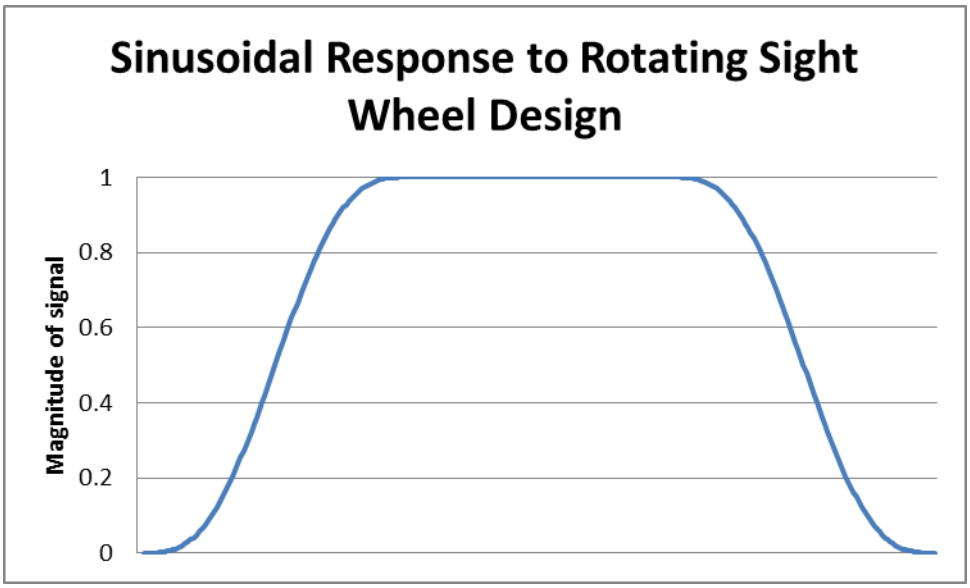

Figure 11: The magnitude of the response of the signal due to the filtering by the sight wheel. Magnitude is multiplied the maximum signal to give the actual signal at a certain point in the rotation cycle.

In order to rotate this sight wheel, a drive train was designed. The sight wheel itself was designed with toothed edges such that it could be drive by a simple gear-driven motor. The drive train was designed specifically for the ultra-high temperature induction furnace which was to be used in research. A mounting system was designed which allowed for a small geared motor to be mounted next to the sight, itself. The sight gear would be driven by this motor at 120 Hertz (two rotations per second). With this drive, given the temporal resolution of the pyrometer at 100 samples per second, 50 samples would be taken per revolution of the sight gear. Thus, approximately 23 samples would be taken per sample per resolution, given the brief blank period used for spacing between samples. The final complete sighting drive-train design can be seen in a solid model rendering in Figure 12 and a photograph of the prototype in Figure 13.

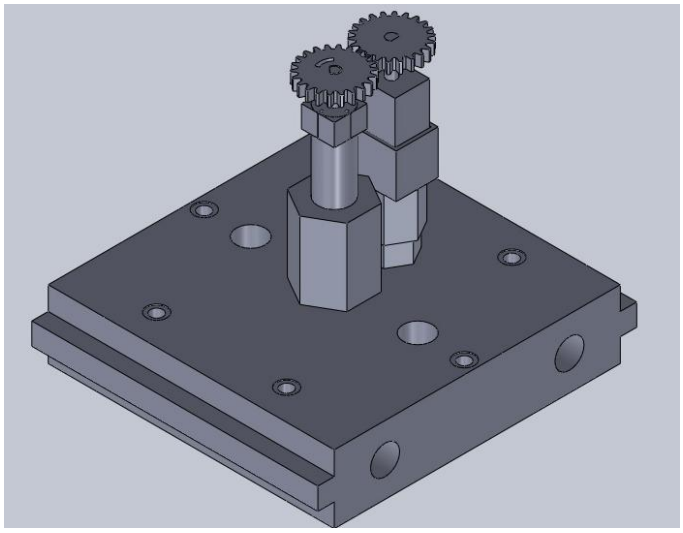

Figure 12: A solid-model render produced in SolidWorks software showing the sighting driving train mounted to the top cap of the reactor. The sight wheel is mounted to the center port. The drive motor is mounted on the nut above the port directly to the right.

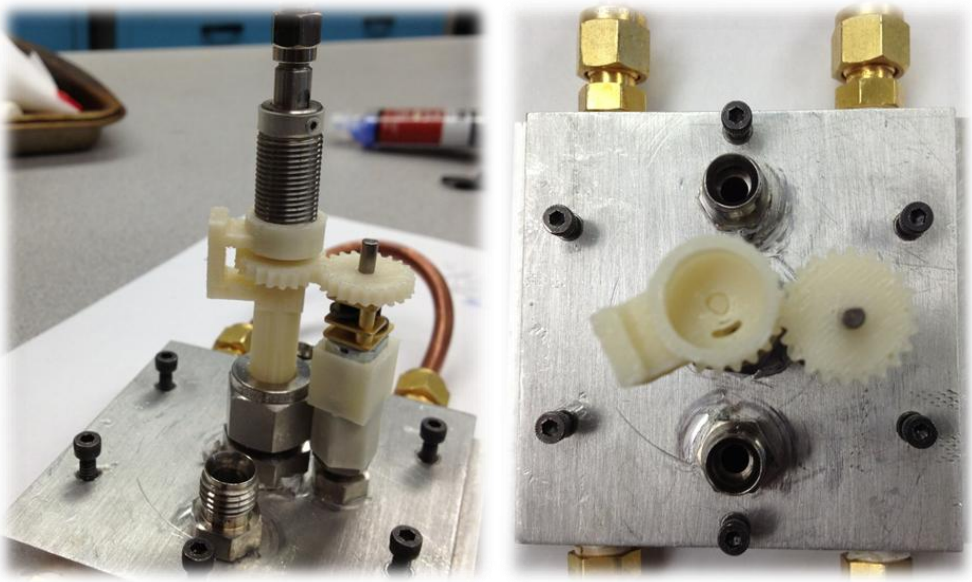

Figure 13: A pair of images of the 3D printed drive train assembly mounted on the reactor cap during test

4 Results

4.1 Thermal Modeling

An enormous amount of thermal modeling was performed in conjunction with the physical testing and design portion of this project. Thermal modeling was performed using ANSYS Icepak Software and COMSOL Multi-physics Software with Heat Transfer Module. Two main areas were examined. First, the effect of the reactor's heating rate on the sample temperatures was examined. Second, the ratio of the mass of the samples with respect to the molybdenum sample cups was examined.

4.1.1 Icepak and COMSOL Geometry and Problem Set-up

A geometry was constructed which reflected the software's best approximation of the reactor's experimental set-up. A "cabinet" was inserted with dimensions of 0.0127m by 0.0127m, representing a similar sized contained to the cylindrical inner-crusceptode, with a radius of 0.0127m. Inside the cabinet, four ellipsoid objects were created with radii of 0.00238m to represent the four samples in the crusceptode. Pairs of opposite ellipsoid were each assigned the material properties of either alumina or silica. A second set of ellipsoids was inserted with the same center points as the four sample ellipsoids. These were given a slightly larger radius 0.0023875m, to give a shell thickness of 0.015mm, the same thickness of the molybdenum foil to be used in physical testing. Material properties were researched and were programmed into the

problem set-up as functions of time where available, when available, or as static values when variable parameters were not available. [20-29]

Finally, five walls were added to the sides of the cabinet to serve as the heat sources. The temperature of these walls was defined to be linked to the outside ambient temperature. This outside ambient temperature could be defined in the "basic problem set-up." This temperature was defined as a transient function of time. Thus, the temperature of the walls could be controlled as a function of time to reflect the similarly isothermal walls of the molybdenum crusceptode. A screen-capture of the geometric set-up of the problem is presented in Figure 14.

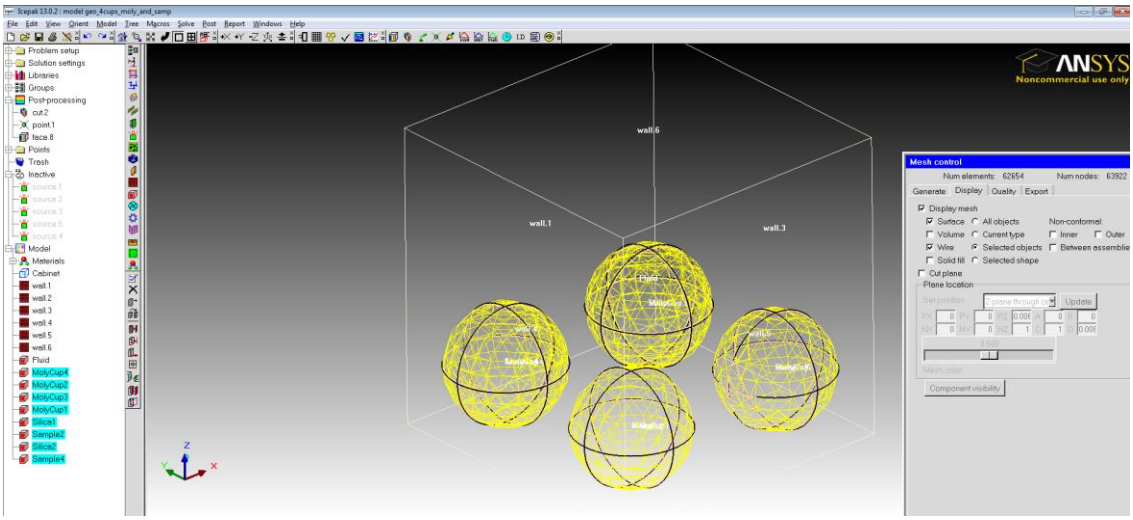

Figure 14: Geometric setup of Icepak software. The four samples are modeled as spheres inside a heated cabinet, which represents the crusceptode.

Geometries used in COMSOL were imported directly from CAD models of the crusceptode and sample cups. COMSOL geometric setup is shown in Figure 15. The

problem was set up using COMSOL's transient analysis, to examine the system changing over a described time interval. The materials were defined using the same values used in the Icepak simulation. The heat transfer was analyzed using the COMSOL heat transfer module using radiation analysis between surfaces.

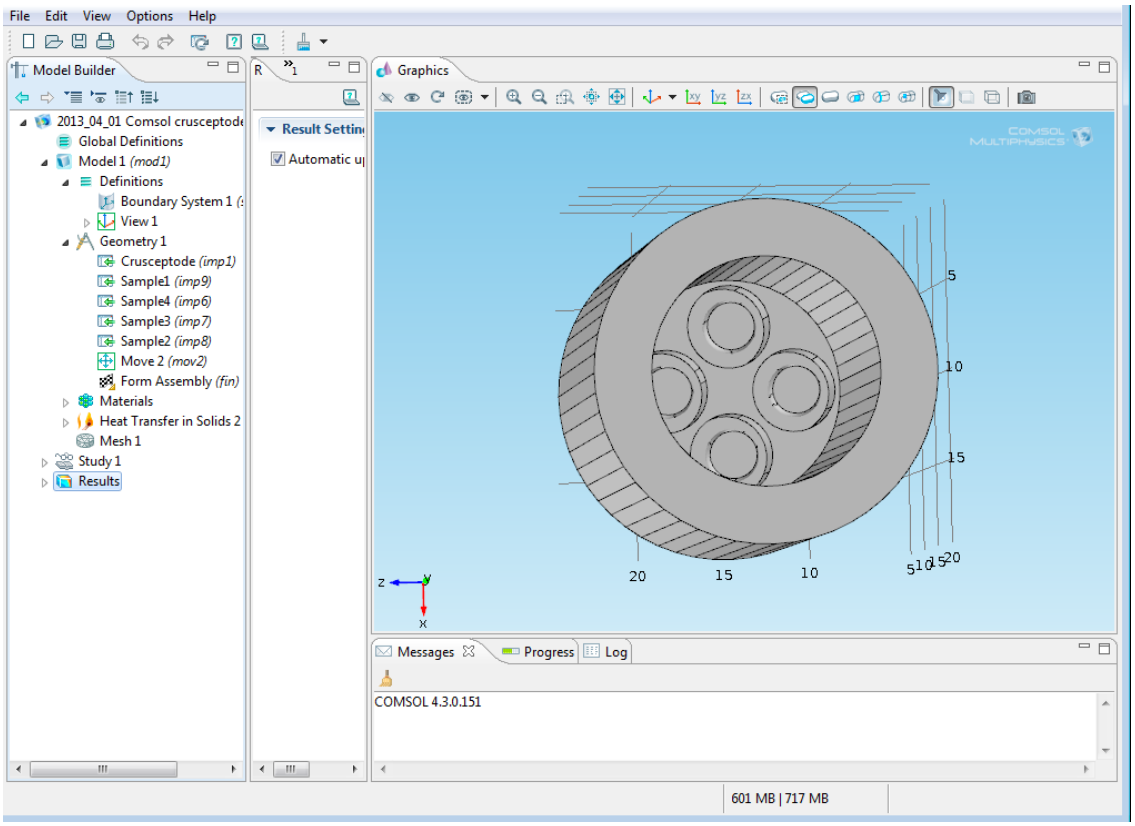

Figure 15: COMSOL Multi-Physics geometric problem setup. The CAD imported geometry used in simulation can be seen above.

4.1.2 Numerical Analysis of Transient Radiative Heat Transfer as a Function of Reactor Heating-Rate

First, the effect of the heating-rate of the reactor was examined with regards to its effects on the sample temperatures and heating rates. In order to examine this, a transient radiative heat transfer problem was set up in ANSYS Icepak.

In total, 11 heating rates were considered, ranging from 0.1°C/sec to 5°C/sec. For each of these heating rates, full, numerical, transient solutions for the entire geometry for temperatures ranging from 23°C to 2600°C were calculated. Transient set-up can be seen in Figure 16.

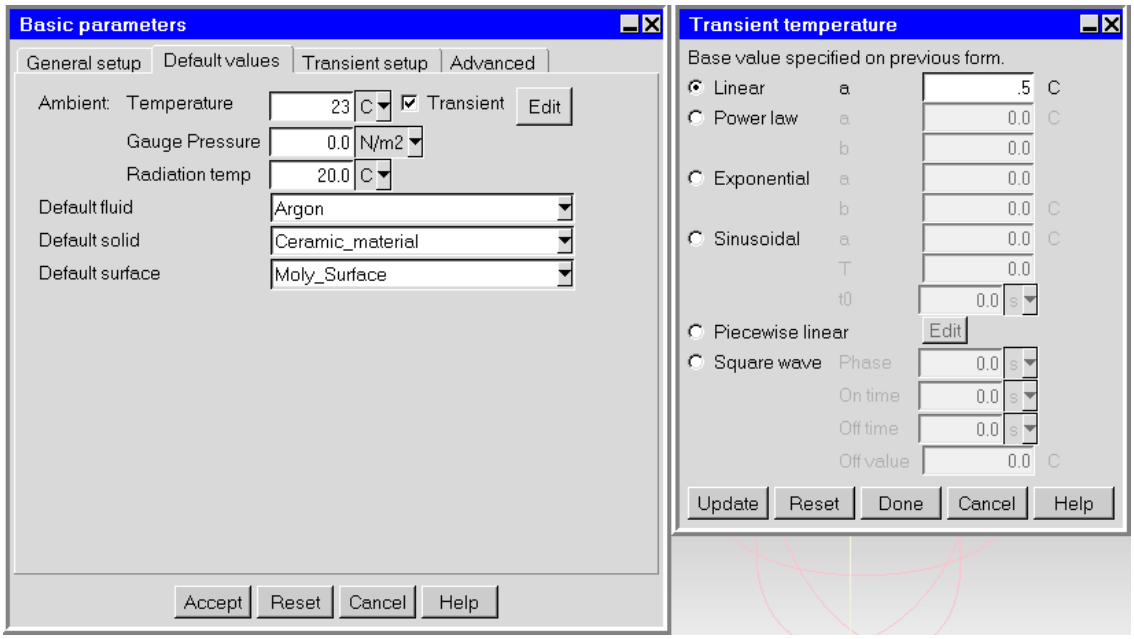

Figure 16: Transient problem set up in ANSYS Icepak for a heating rate of 0.5°C per second.

In order to examine the effect of the heating rate on the sample temperatures, the temperature of three points were recorded and stored in a .CSV file over the length of

the heating. One point was defined as being on the molybdenum crusceptode wall (which reflects the exact heating rate), one point was defined as being in the center of the silica sample, and one point was defined as being in the center of the alumina sample. The resulting figures are presented in Figures 17 and 18, in which the thermal contours of the inner crusceptode can be seen at an initial isothermal state, at $t = 0$, and at a state later in the transient heating in which the reactor wall is at a temperature of approximately 1130^{o}C.

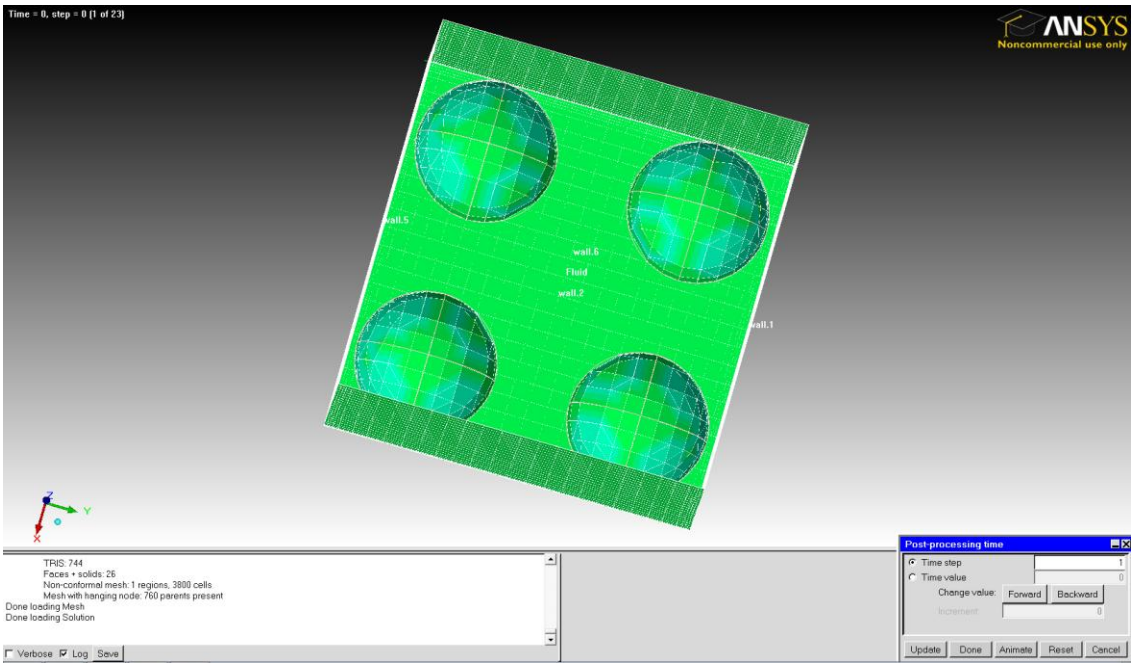

Figure 17: ANSYS Icepak software problem geometry at an initial time at which the crusceptode and samples are in thermal equilibrium at room temperature.

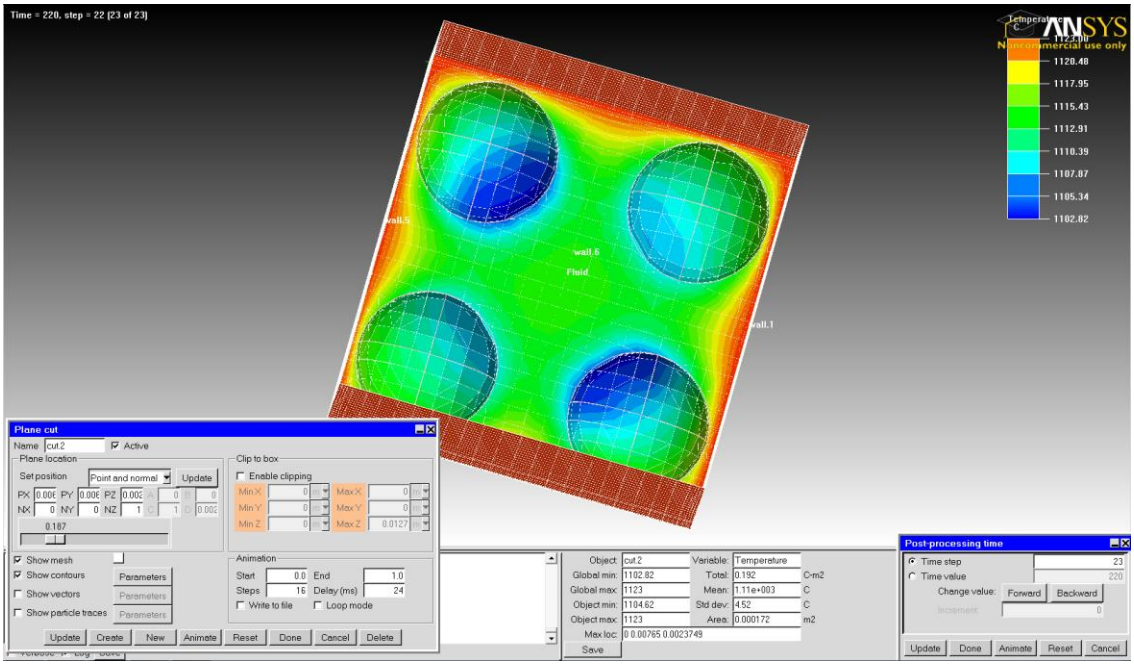

Figure 18: ANSYS Icepak software problem geometry at a time later in the transient problem at which the crusceptode and samples are being heated by radiation from the reactor walls at approximately 1130^{o}C. A section cut is being displayed which shows the thermal contours of the space surrounding the samples.

For each heating rate, the difference in temperature, dT, between each sample (silica and alumina) and the temperature of the molybdenum crusceptode wall was plotted as a function of time. These dTs were plotted as a function of reactor temperature, producing two plots for each heating rate. These data were calculated without taking a melt-plateau into account in order to establish an overall trend. A trend line was added using Microsoft Excel to these data. For all heating rates, the trend line which best matched this temperature difference, dT, increased exponentially with temperature. An example of these plots can be seen below in Figure 19, where the sample dTs are plotted as a function of reactor temperature for a heating rate of 1^{o}C/second.

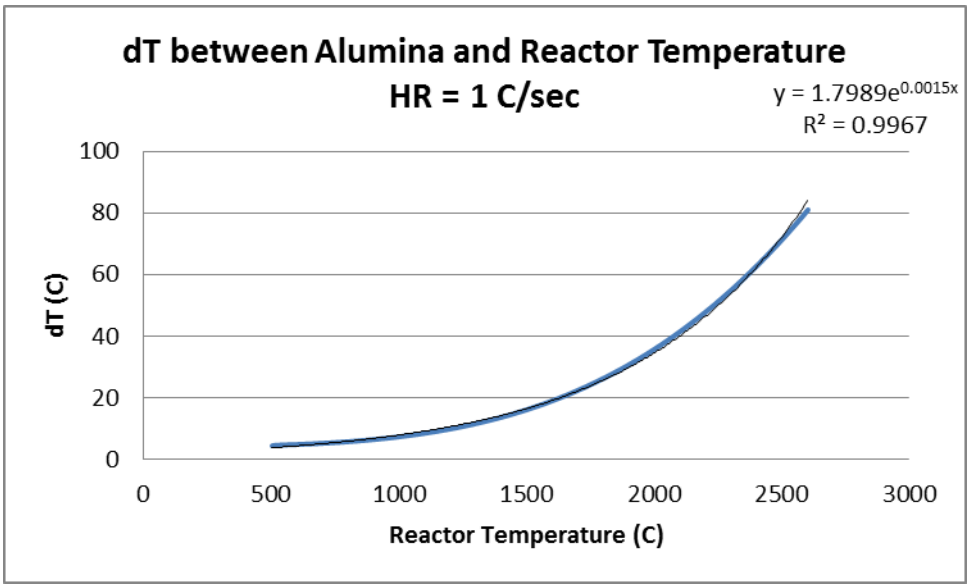

Figure 19: A plot of temperature difference between an alumina sample and reactor temperature at a constant heating rate of 1°C per second (blue line). A trend line (black line) was added with the equation $y = 1.7989e^{0.0015(x)}$ which gives an $R^2 = 0.9967$.

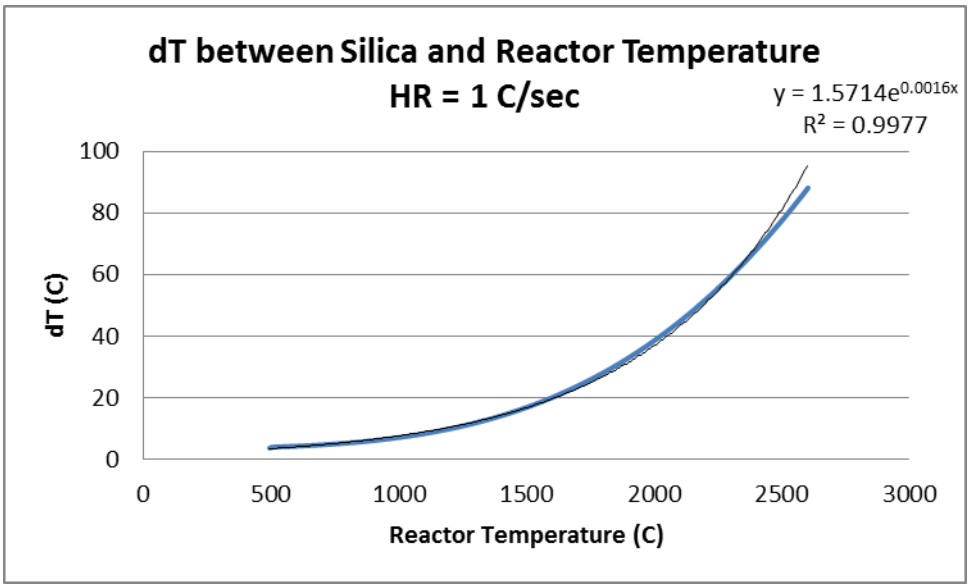

Figure 20: A plot of temperature difference between a silica sample and reactor temperature at a constant heating rate of 1°C per second (blue line). A trend line (black line) was added with the equation $y = 1.5714\ e^{0.0016(x)}$ which gives an $R^2 = 0.9977$.

A correlation was then established between the exponential function in which the *dT* was predicted from the reactor temperature and the heating rate. In order to do this, the trend line for each *dT* vs. *T* was written in the for $dT = Ae^{b(T)}$ (for alumina) or $dT = Ce^{d(T)}$ (for silica). These coefficients were then tabulated, as can be seen in Table 3 and plotted as functions of heating rate in Figures 21-23.

	Alumina		Silica	
Heating Rate (^{o}C/sec)	**A**	**b**	**C**	**d**
0.1	0.3698	0.0013	0.3042	0.0017
0.3	0.7905	0.0017	0.6497	0.0019
0.5	1.0916	0.0017	0.9283	0.0018
0.7	1.4475	0.0016	1.2628	0.0017
1	1.7989	0.0015	1.5714	0.0016
1.5	2.2824	0.0014	2.0252	0.0015
2	2.0712	0.0014	2.1587	0.0015
2.5	2.4274	0.0014	2.5365	0.0014
3	2.8278	0.0013	2.9501	0.0013
4	2.8071	0.0013	4.0461	0.0013
5	3.5290	0.0012	5.1357	0.0011

Table 3: Exponential coefficients for the function describing difference between sample temperature and reactor temperature, *dT*, as a function of reactor temperature, *T*, for alumina and silica samples, $dT_{alumina} = Ae^{b*T}$ and $dT_{silica} = Ce^{d*T}$

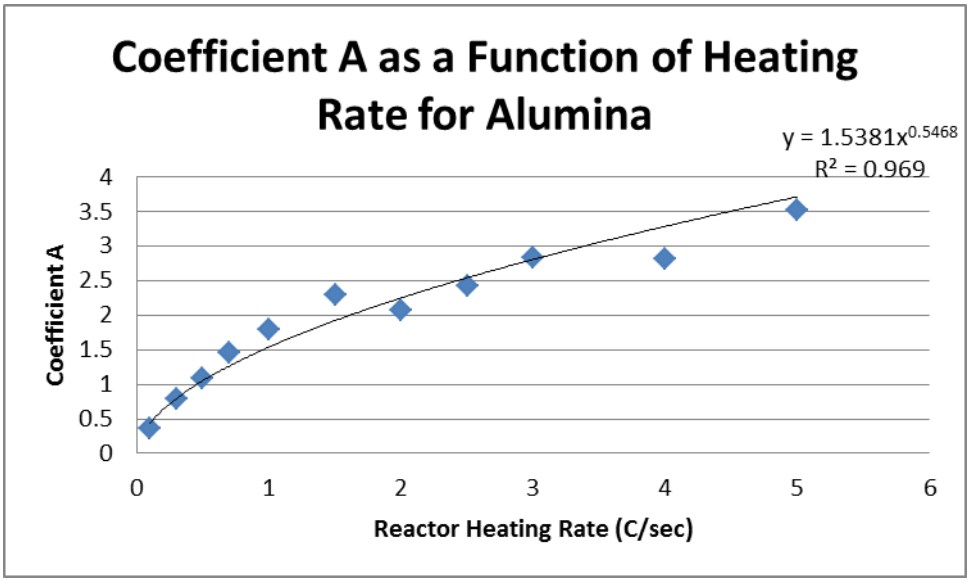

Figure 21: Coefficient *A* as a function of reactor heating rate for a sample of alumina, based on the trials performed in ANSYS Icepak, for the function $dT = Ae^{b*T}$.

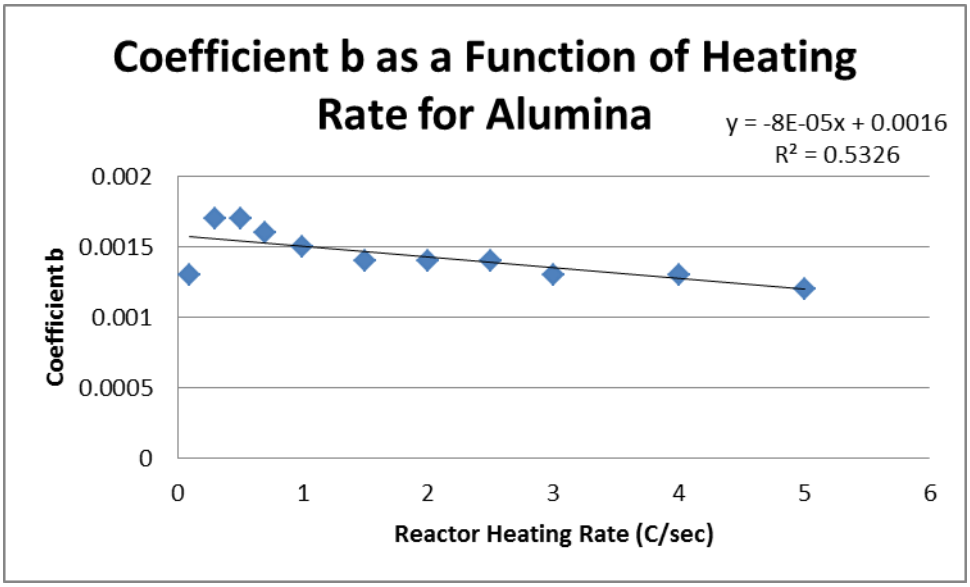

Figure 22: Coefficient *b* as a function of reactor heating rate for a sample of alumina, based on the trials performed in ANSYS Icepak, for the function $dT = Ae^{b*T}$.

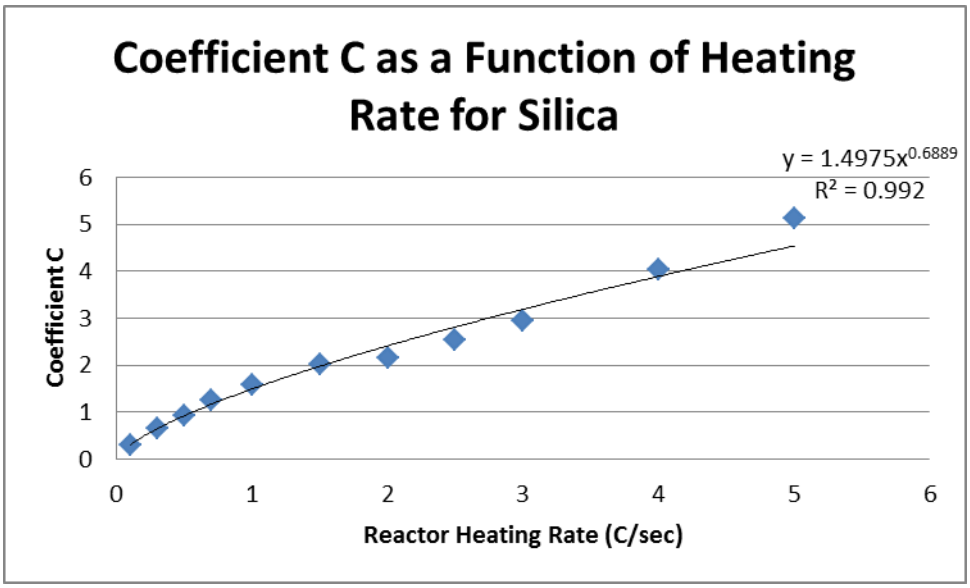

Figure 23: Coefficient *C* as a function of reactor heating rate for a sample of silica, based on the trials performed in ANSYS Icepak, for the function $dT = Ce^{d*T}$.

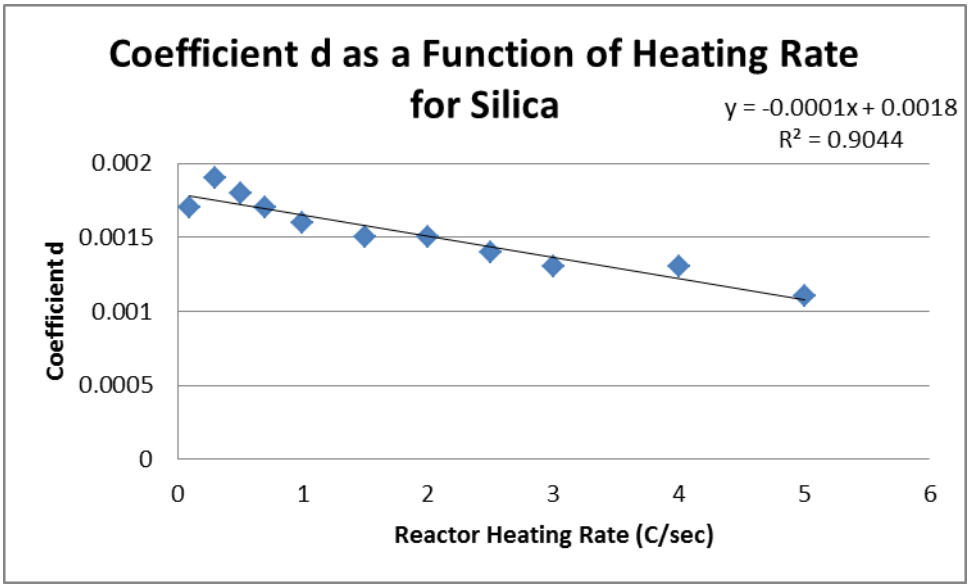

Figure 24: Coefficient *d* as a function of reactor heating rate for a sample of silica, based on the trials performed in ANSYS Icepak, for the function $dT = Ae^{d*T}$.

With these functions, it is now possible to predict the temperature difference between a sample of alumina or silica and the reactor wall at any given temperature at any heating

rate, assuming interpolation. These functions are presented on one plot for each material in Figures 25 and 26.

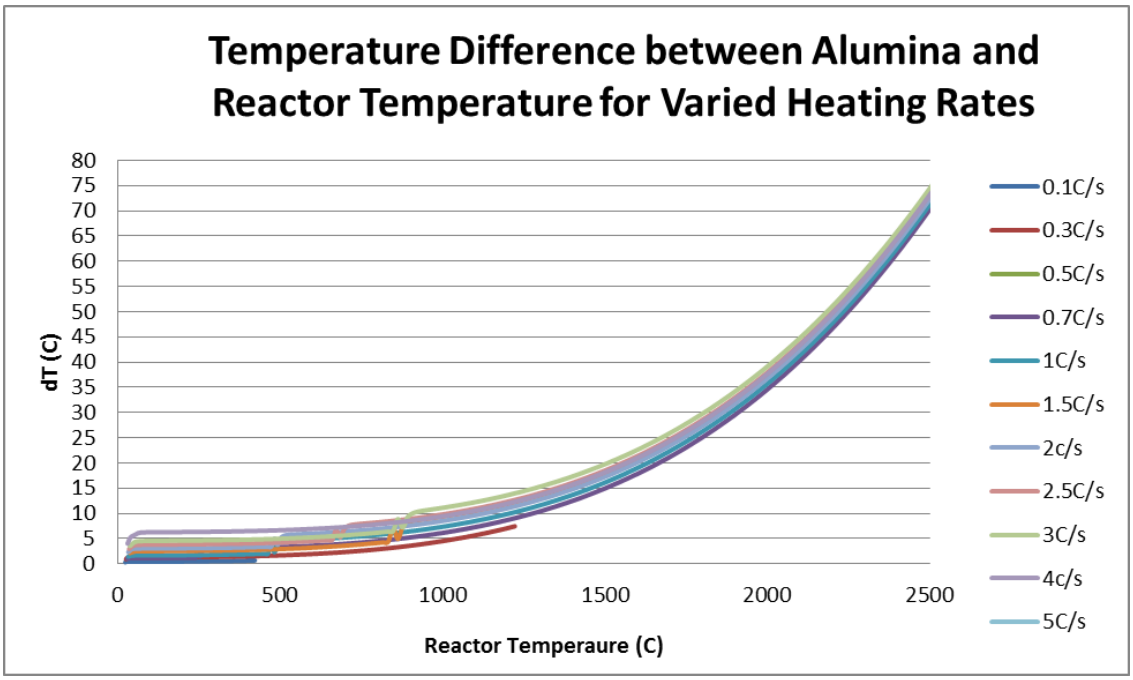

Figure 25: The temperature difference between the alumina sample and the reactor wall temperature as a function of reactor temperature for a variety of heating rates between 0.1^{o}C per second to 5.0^{o}C per second.

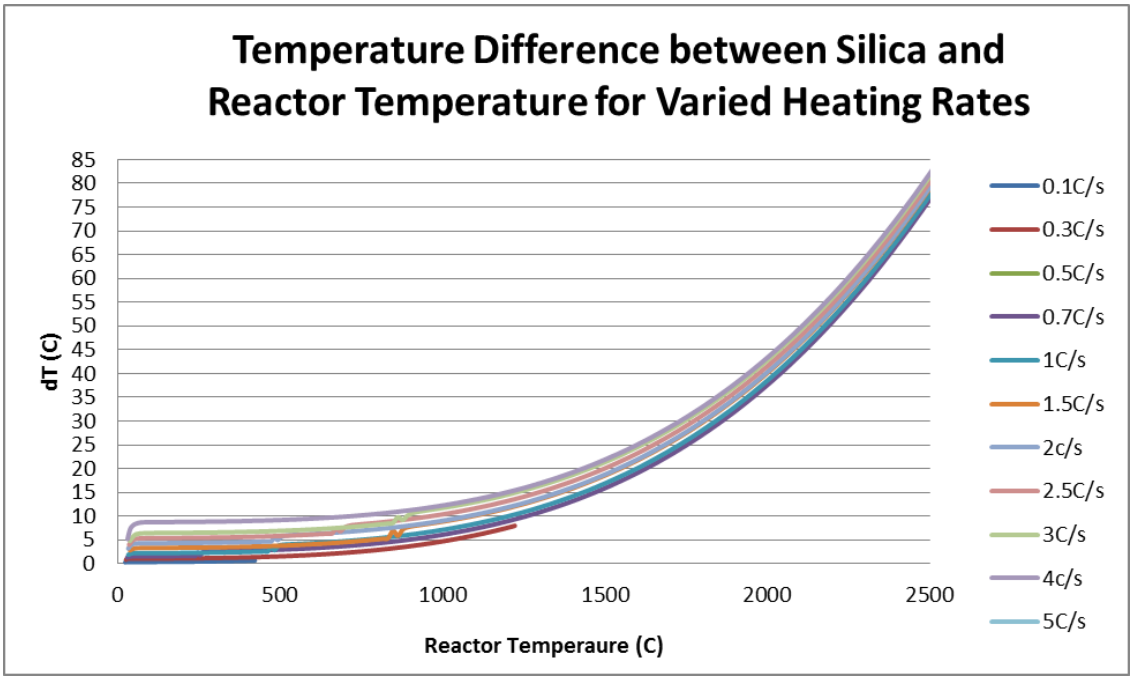

Figure 26: The temperature difference between the alumina sample and the reactor wall temperature as a function of reactor temperature for a variety of heating rates between 0.1°C per second to 5.0°C per second.

Finally, the temperature difference between the two samples during a melt plateau was examined as a function of heating rate. It was desired to examine this value as a function of heating rate to determine if a correlation could be derived between heat of fusion, H_f, and the integrated area under the melt-plateau temperature curve, A.

To accomplish this, the data surrounding the melt-plateau were examined from 1550°C to 1660°C. The difference between the alumina and silica sample was calculated and plotted, seen in Figure 27. The areas under these melting curves were calculated for a variety of heating rates between 0.5°C/sec and 5°C/sec with a constant sample to sample-cup mass ratio of 10:1, and a heat of fusion of 14.0 kJ/mol [30].

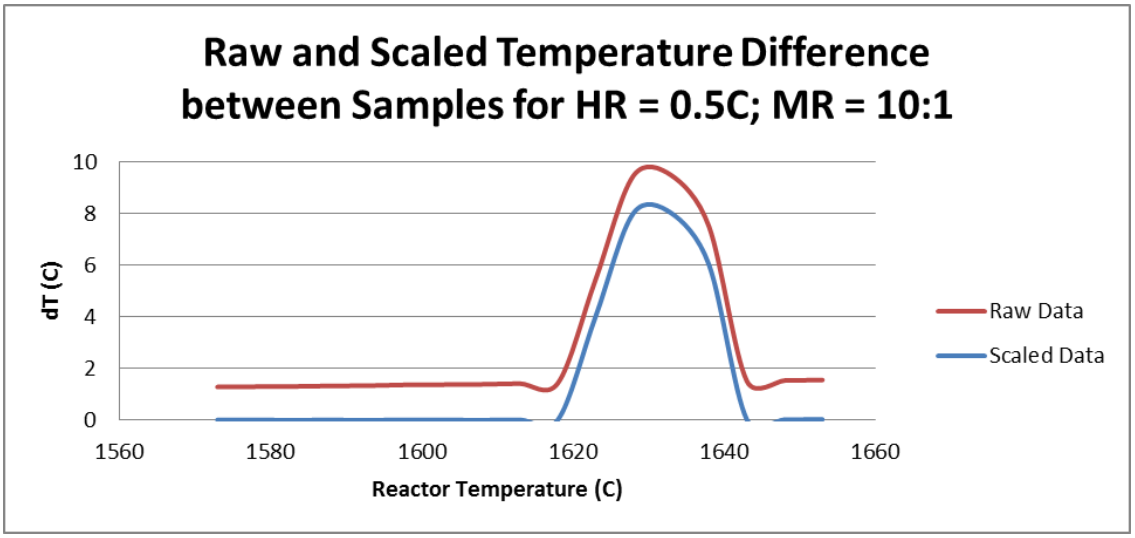

Figure 27: Temperature difference (raw and scaled) between alumina and silica samples around the melt-plateau of silica for a heating rate of 0.5°C and a sample to sample-cup mass ratio of 10:1, as a function of reactor temperature at temporal resolution of 2 solutions per second. The melt occurs at 1600°C and so a thermal lag of approximately 20°C can be observed between the silica sample, itself, and the reactor wall.

Each of these melt-plateau curves was scaled such that the baseline *dT*, the minimum, was scaled to 0. This was accomplished by first establishing an equation to represent the heating rate without taking into account the melt-plateau. The data from earlier in this section were used to predict this heating rate, which was then subtracted from the raw data. Thus, the difference in temperature which was not caused by the melt-plateau was able to be factored out of the data, as also shown in Figure 27. Integration was then performed to determine the area under the remaining curves. The resulting values were plotted in Figure 29. The data were determined to be essentially steady state, with a constant scale relating the area under the melt-plateau curve, *A*, to heat of fusion, $H_{f,}$ as a function of heating rate, given the equation,

$$Hf = 0.3206\, A.$$

This correlation was determined by calculating the average of all the integration areas, with a +/-7.3% variation around this average. Due to this error, the simulation was re-run with a higher temporal resolution of 50 solutions per second around the melt-plateau, which resulted in a significantly smoother curve, as seen in Figure 28, in which both the raw and scaled data are shown for a heating rate of 0.5°C/sec and a sample to sample-cup mass ratio of 10:1. This integration process was repeated for 5 other heating rates. A new and more accurate correlation was thus determined by averaging these integration areas, yielding,

$$Hf = 0.2983\ A.$$

As seen in Figure 29, a significant increase in consistency was found in the data from the higher temporal resolution simulations, where variation of only +/- 0.9% was observed.

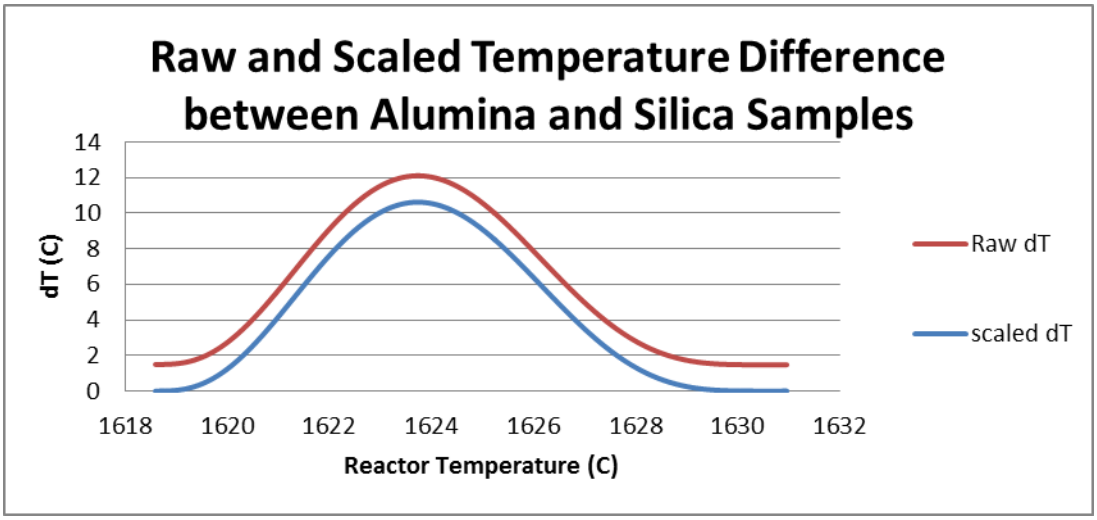

Figure 28: The raw and scaled temperature difference between alumina and silica samples around the melt-plateau of silica for a heating rate of 0.5°C and a sample to sample-cup mass ratio of 10:1 and a heat of fusion of 14.0 kJ/mol, as a function of reactor temperature with a temporal resolution of 50 solutions per second. The melt occurs at 1600°C and so a thermal lag of approximately 20°C can be observed between the silica sample, itself, and the reactor wall.

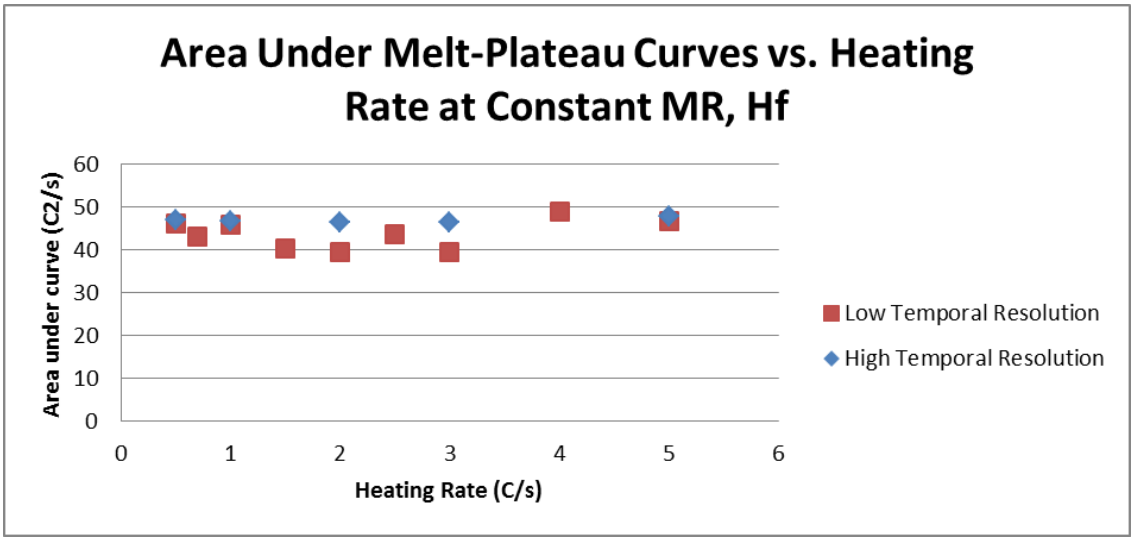

Figure 29: The resulting values of the areas under the curves of the scaled melt-plateau graphs for heating rates of 0.5°C to 5.0°C and a constant heat of fusion of 14.0 kJ/mol and sample to sample-cup mass ratio of 10:1, as a function of reactor temperature for both low (red) and high (blue) solution temporal resolutions.

4.1.3 Analysis of Sample to Sample-Cup Mass Ratio

The effect of the mass of the sample and the mass of the molybdenum sample cup were also examined using COMSOL Multi-physics software. In this examination, a similar problem set-up was used as was described in Section 4.1.1. Instead of varying the heating rate in this model, however, the geometry of the problem was varied and the heating rate was kept constant at 0.5°C/second.

First, a base-line simulation was run in which the sample to sample-cup mass ratio was infinite, or a massless cup. This was established by simply setting the sample-cup's shell thickness to 0 and running the simulation. As in the previous simulations, the

temperature data from three points (the molybdenum crusceptode wall, the center of the alumina sample, and the center of the silica sample) were recorded and stored in .CSV files. These values were plotted as a function of reactor temperature as seen in Figures 30 and 31.

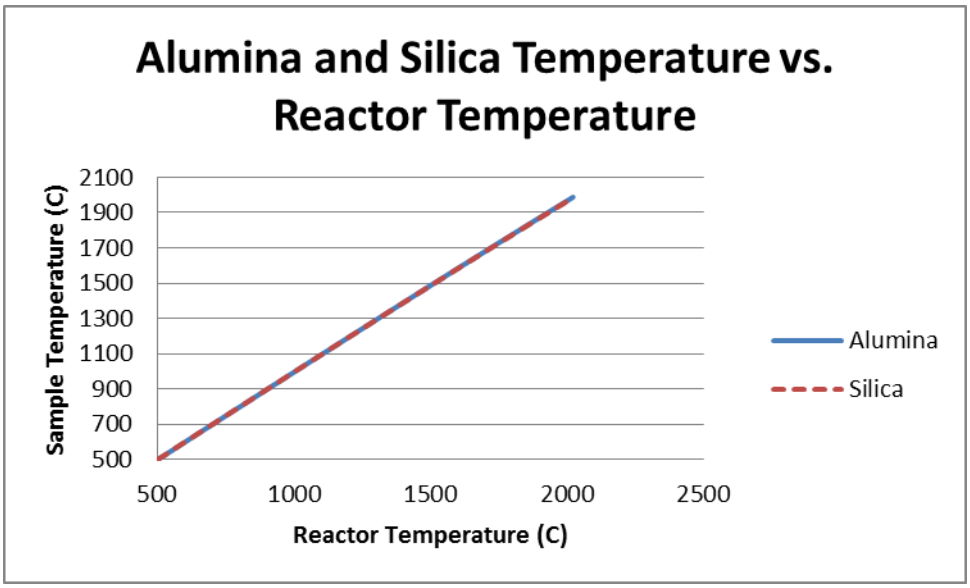

Figure 30: Alumina and silica sample temperatures as a function of reactor temperature at a heating rate of 0.5^{o}C per second and a sample-cup thickness of 0 (a sample to sample-cup mass ratio of infinity). These data would serve as the standard against which other mass-ratios were compared

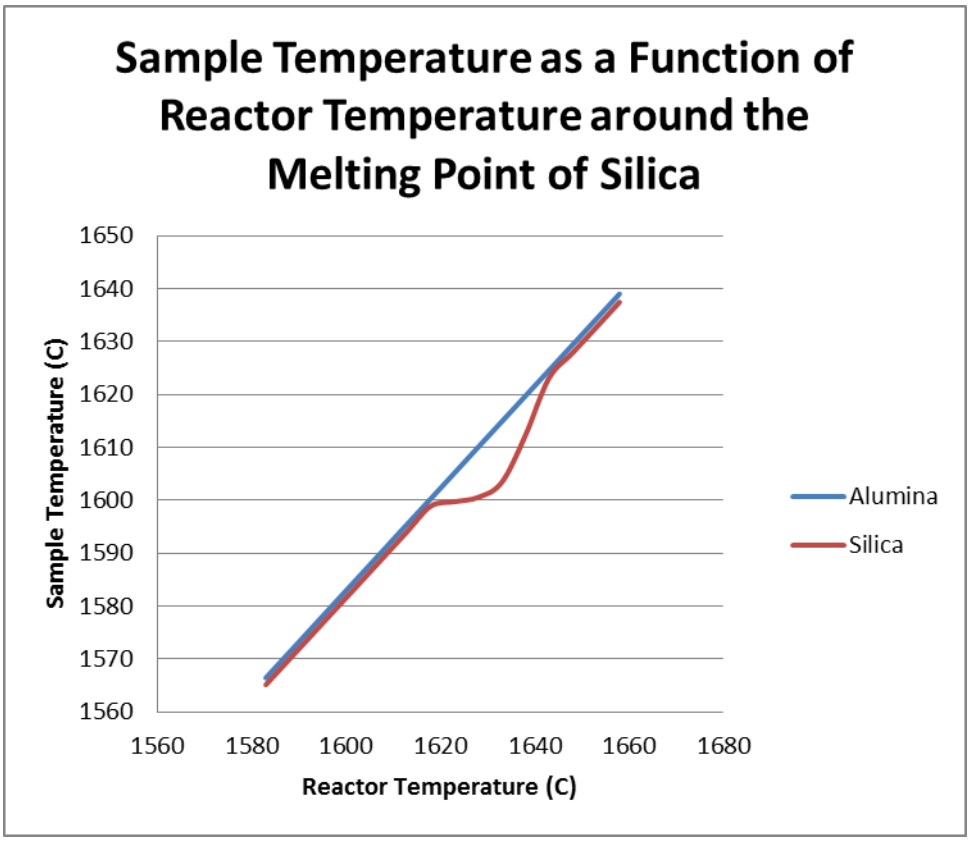

Figure 31: Alumina and silica sample temperatures as a function of reactor temperature at a heating rate of 0.5°C per second and a sample-cup thickness of 0 (a sample to sample-cup mass ratio of infinity). A close-up of the melting plateau of silica is shown in these data, from whence the maximum sample dT is calculated.

Using the infinitely thin sample-cup as a standard against which other simulations could be compared, the simulation was repeated with various sample geometries, reflecting different sample to sample-cup mass ratios, while keeping the heating rate and all other conditions the same.

The same three points in the results of these simulations were stored as .CSV files and examined in Microsoft Excel. The difference in temperature between each sample's temperature in that simulation and the accepted temperature from the first standard

simulation was calculated and plotted as a function of reactor temperature. An example of this can be seen below in Figure 32.

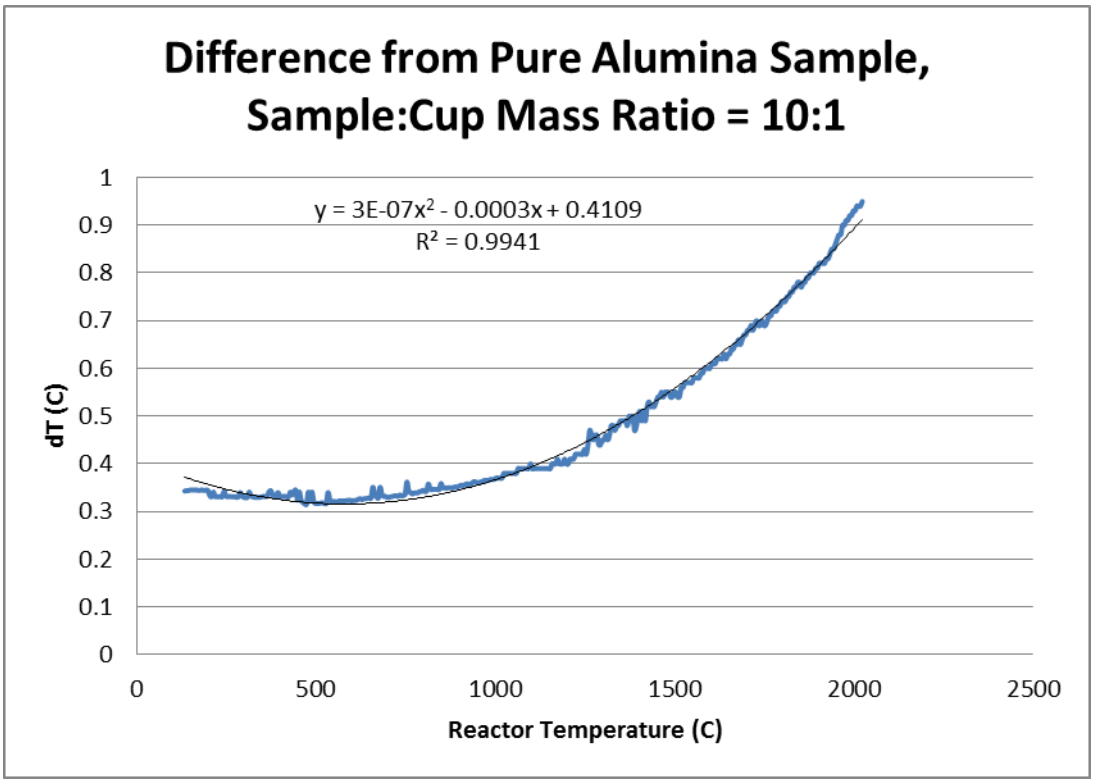

Figure 32: The difference in temperature between the standardized alumina sample and the alumina sample used in the simulation, with a sample to sample-cup mass ratio of 10:1 and a heating rate of 0.5°C/sec. Simulation data are in blue, trend-line data are in black.

A trend-line was added to these data. The best fitting trend line was determined to be a second order polynomial equation of the form,

$$y = Ax^2 + Bx + c$$

Equation 3: Second order polynomial equation to describe deviation from standardized data.

which yielded an R^2 value of 0.9941 for the above example. Due to very small differences in the values of *A* and *B* for the various mass ratios, the value of *c*, dubbed the difference coefficient, from the above equation was selected as the best reflection of the magnitude of the deviation from the accepted standard, and was thus tabulated below in Table 4 and plotted in Figure 33 A clear exponential trend can be seen in these data, below, where difference coefficient decreases exponentially with increasing sample to sample-cup mass ratio.

Sample to Sample-Cup Mass Ratio	**Alumina Difference Coefficient, *C***	**Silica Difference Coefficient, *C***
10:1	0.4109	1.052
5:1	1.501	2.5037
2:1	1.6496	3.4851
1:1	8.31	9.17

Table 4: The difference coefficients, *C*, for both Alumina and Silica samples as a function of mass ratio. These values reflect the deviation of a sample based on the cup thickness from the behavior of a sample with a theoretical cup thickness of zero.

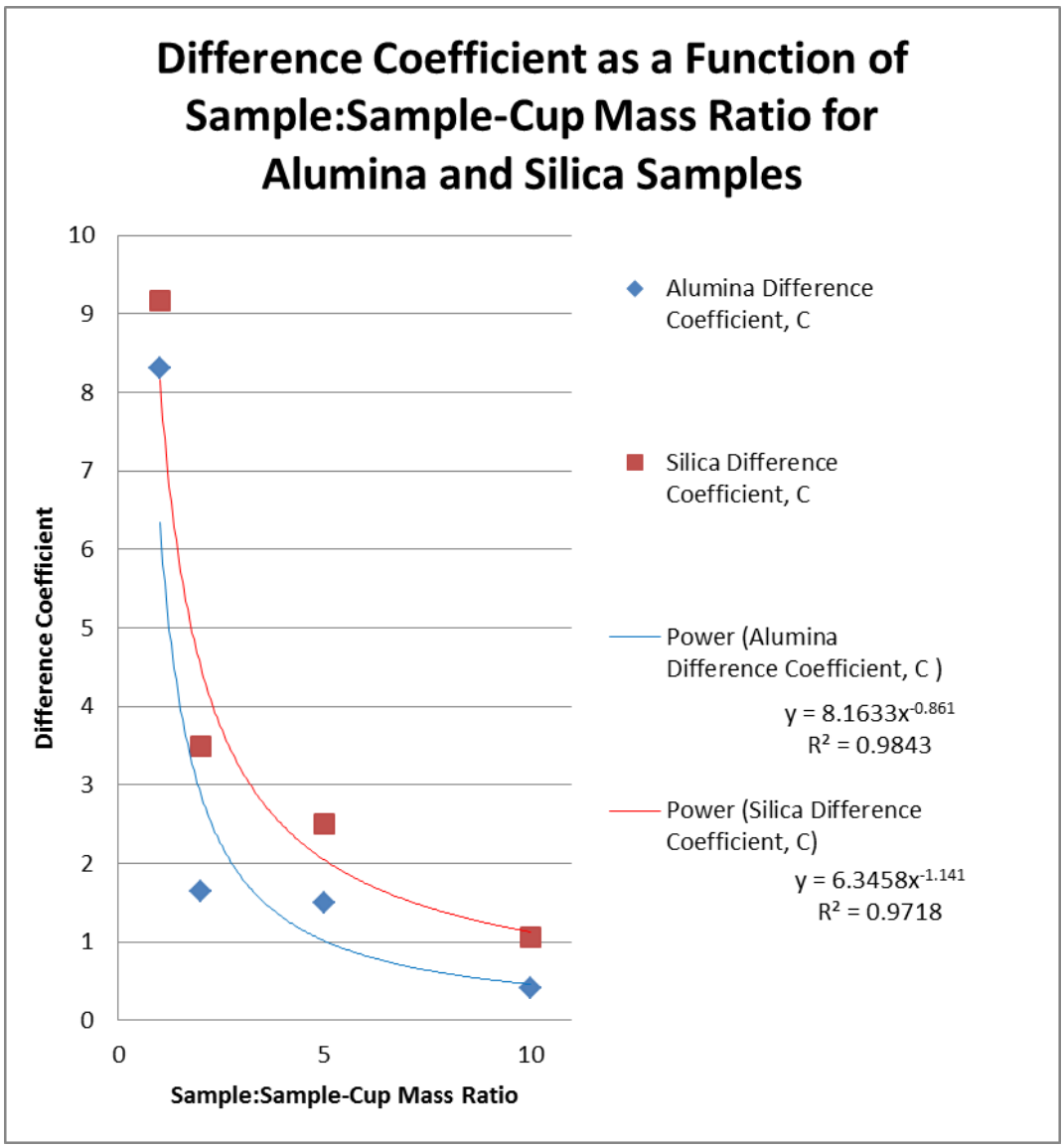

Figure 33: Difference coefficient as a function of sample to sample-cup mass ratio. Simulation data points are red (silica) and blue (alumina); trend lines are solid red (silica) and blue (alumina)

The maximum change in temperature during the melt plateau was also examined from these data. In Microsoft Excel, the difference between the two sample temperatures was calculated at every point. An example of these data is plotted below in Figure 34. The maximum difference between the two samples during the melt was tabulated and

plotted for each sample to sample-cup mass ratio. These data are presented below in Table 5. These data are also plotted in Figure 35, where a trend-line was added, showing a strong exponential increase in maximum temperature difference with increasing sample to sample-cup mass ratio.

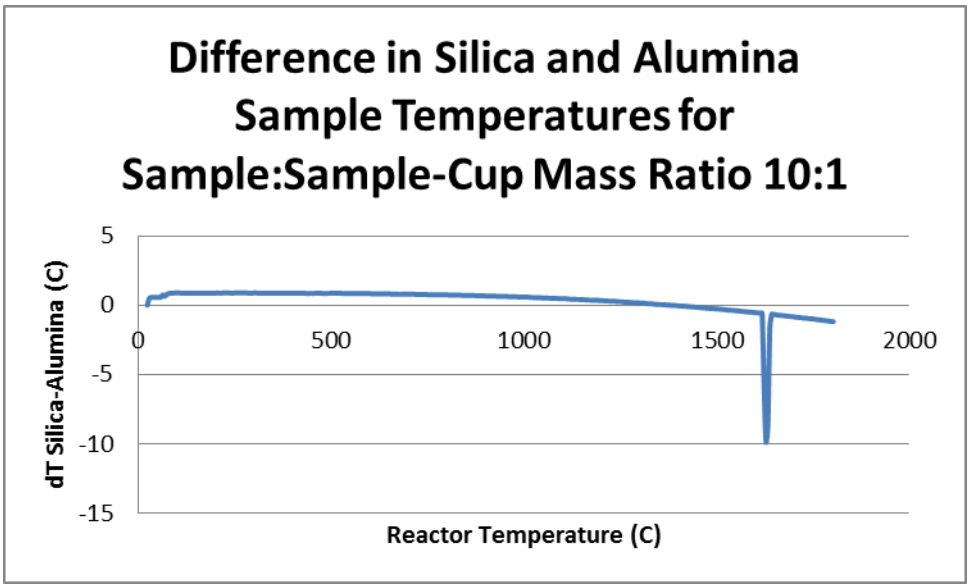

Figure 34: The difference in sample temperature between a silica and an alumina sample, for a sample to sample-cup mass ratio of 10:1. A large negative spike can be seen with an onset at 1600^{o}C at the melting point of alumina.

Sample to Sample-Cup Mass Ratio	Max dT between Samples During Melt
10:1	9.87
5:1	1.97
2:1	0.41
1:1	0.03

Table 5: The maximum difference between alumina and silica samples durnig the simulated melting of silica given a varying sample to sample-cup mass ratio.

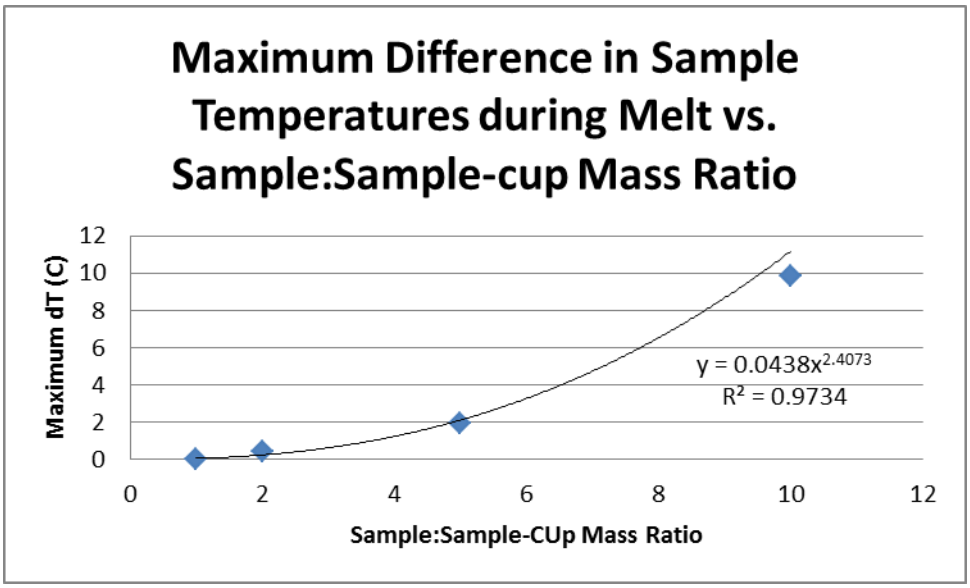

Figure 35: The maximum difference in temperature between alumina and silica samples during the simulated melting of silica as a function of sample to sample-cup mass ratio. Simulation data are represented as blue points; trend-line is represented as solid black.

4.2 Experimental Results

Two physical tests were performed as of the time of writing of this report (April, 2013). The results of these tests are presented below.

4.2.1 Test I: Hand Calibration of Sighting Drive Train

A simple proof of feasibility test was the first physical test performed using the previously designed apparatus. In this test, the sighting wheel and pyrometer were to be tested to determine whether the wheel could effectively filter incoming radiation. To accomplish this, a high-power incandescent bulb was used as a bright radiation source, on which the pyrometer could be sighted.

First, the pyrometer was attached to the computer for digital sample at 100 samples per second. Next, the fiber-optic cable was attached to the pyrometer box and the head of the fiber-optic cable was attached to the sighting tube. Data-logging was started and the pyrometer head was then pointed in the direction of the incandescent bulb. The sighting-wheel was then spun by hand, slowly, at a rate of approximately 15 rotations per minute.

The results of this test are presented in Figure 36. A clear on-off pattern can be seen in these data. These results are interpreted in full in the Discussion section, Section 5, of this report.

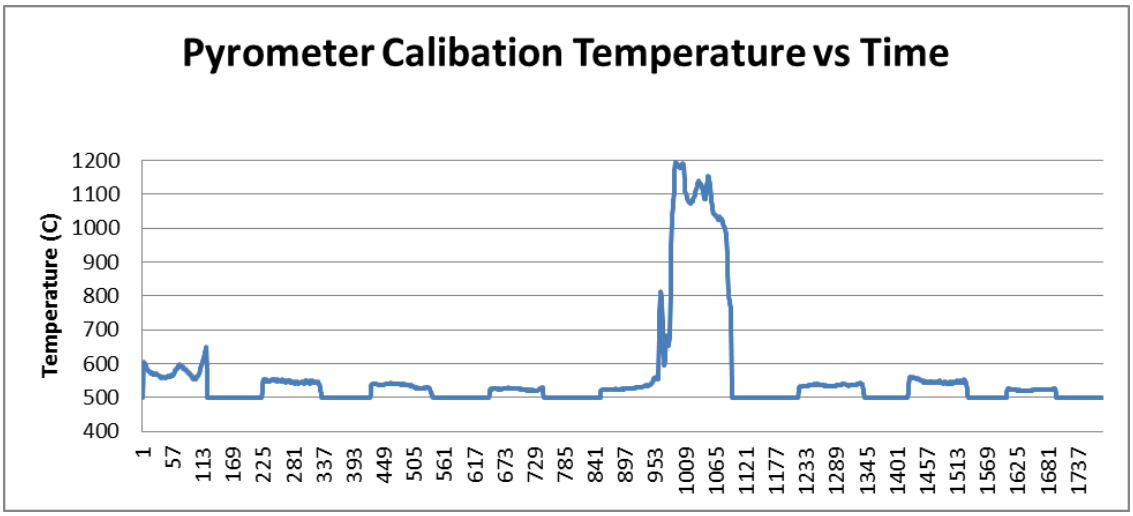

Figure 36: Data from the pyrometer calibration test in which the sight wheel was drive slowly, by hand. Four distinct samples can be seen, with clear stop period between each sample.

4.2.2 Test II: High-Temperature Thermocouple-based DTA

In the second test, high temperature DTA was tested on the scale of this project. In this test, however, temperature measurement was conducted using type-C thermocouples as opposed to non-contact pyrometry. The test was conducted using thermocouples in an attempt to confirm the results of numerical analysis performed in thermal modeling simulations discussed in Section 4.1.

The experiment was performed using the ultra-high temperature induction furnace. Two samples were prepared to be melted. Aluminum oxide (alumina), in the form of high-purity aluminum oxide bubbles, was used for sample #1. Silicon dioxide (silica), in the form of crystalized silica frit, was used as sample #2. These samples were placed into two molybdenum sample-cups, whose masses were measured using a high-accuracy milligram scale before sample insertion. The sample-cup masses were determined to both be 5.53mg +/- 0.03mg. The alumina sample was measured to have a mass of 9.50 mg +/- 0.01 mg. The silica sample was measured to have a mass of 10.04 mg +/- 0.01 mg.

The sample-cups, with samples inside, were then inserted into two opposite holes in the custom molybdenum crusceptode. The crusceptode was then lowered into the center of the reactor.

After some difficult, the thermocouples were successfully inserted into the samples. With one thermocouple in each sample, the pyrometer gathering data directly from the

crusceptode, and a third thermocouple mounted on the inner heat shield, the test was initiated. The reactor was heated at a rate of 1 to 2^{o}C per second using a custom-designed LabVIEW control interface.

Approximately 820 seconds into the experiment, with the samples at a temperature of approximately 1632^{o}C, a failure occurred in both type C thermocouples, where the reported temperature dropped to a reading of approximately 35^{o}C. There were several brief periods where the Lepel power was turned off and it appeared that the thermocouples were reporting accurate data, but upon the starting of the returning of the Lepel to its previous power level, the data reported were once again in the 30-40^{o}C range. Consistent accurate data were not returned until the samples reached a temperature of approximately 2000^{o}C at an experiment time of approximately 1170 seconds, at a Lepel power level of 55%.

From this point on, the reactor was brought to a high temperature of approximately 2300^{o}C, for which a temperature drop of approximately 100^{o}C was observed between the temperature of the molybdenum crusceptode and the alumina sample. The Lepel power was then turned off, allowing the reactor to cool through the solidification of both the alumina and the silica samples. However, as the reactor approached the temperature range of interest for the silica sample (around its melting point at 1600^{o}C), the data from both of the type-c thermocouples once again failed to report accurately, reporting temperatures in the 30-40^{o}C range once again. The reactor was then heated again up to 2300^{o}C, and allowed to cool to examine if the thermocouples would fail

once again. This was confirmed, as the thermocouples both failed at a similar temperature of around 1700^{o}C.

Thus, it was decided to examine the melt plateau of alumina, since the thermocouples appeared to be providing reasonable and accurate data in that temperature range. A total of six trials were performed in which the samples were brought above the melting temperature of alumina, at 2072^{o}C, and then allowed to cool. A significant differential was noted between the two samples in both the heating and cooling phase in each trial.

In trails #1, 2, 3, 4, and 6, the sample was allowed to cool naturally, by turning the Lepel power to 0, resulting in a very rapid cooling process. In trail #5, the Lepel power was stepped down slowly, to attempt to simulate a slower cooling rate. This trial also featured the lowest maximum dT (the maximum difference between the alumina and silica sample temperatures during the melt) at 70.387^{o}C. The average of the maximum dT for all six trials was 100.5862^{o}C. This is significantly higher than the average dT during the heating process, which was determined to be 16.588^{o}C. These data are presented below in Table 6 and the full temperature curves of each trial have been overlaid, visible in Figure 37. Each individual trial is presented in Appendix Figures 2-7.

Trial #	Max dT (^{o}C)	Average Maximum dT (^{o}C)
1	86.45	100.8562
2	120.043	
3	116.308	
4	124.043	
5	70.387	
6	87.906	

Table 6: The maximum difference in temperature between alumina and silica samples during the six trials through the melt plateau of alumina between 2000^{o}C and 2100^{o}C. All the temperature vs. time plots for each of these trials is presented below, and each individual trial is plotted individually in Appendix Figures 2 through 7.

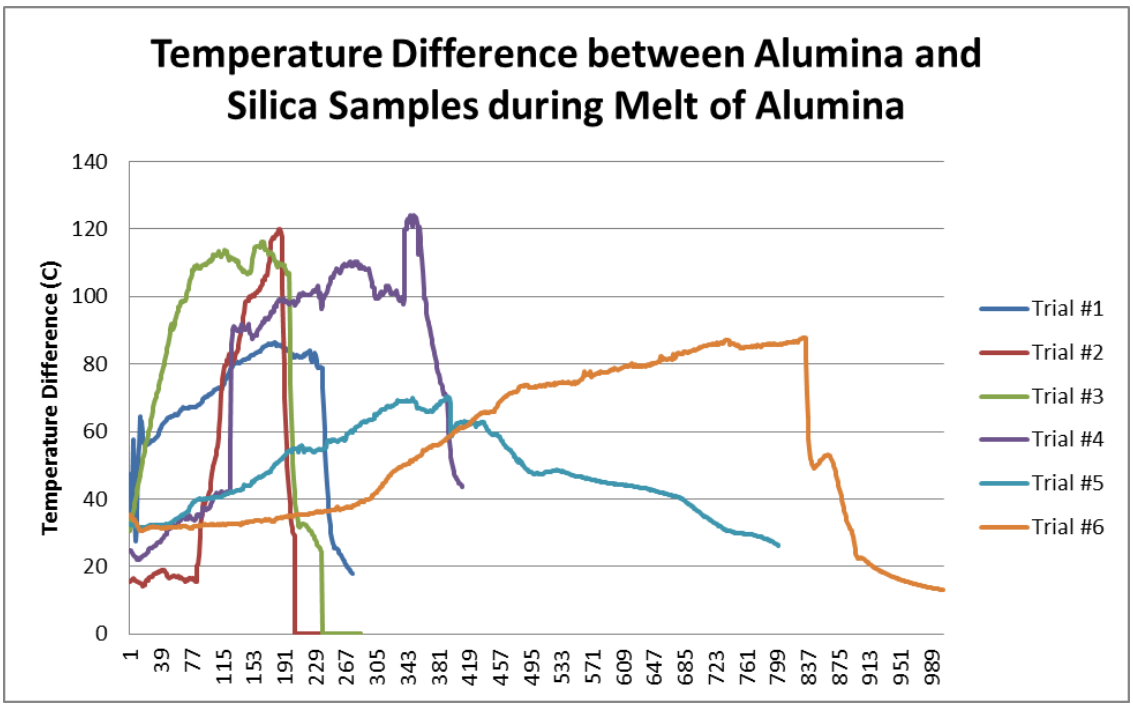

Figure 37: An overlay of the six trials of heating and cooling of alumina through its melt plateau. The difference in temperature between alumina and silica samples is represented by each curve. The x-axis is sample number since the beginning of that trial, with two samples being taken per second.

The implications and interpretation of this test are discussed in the following discussion, Section 5.

5 Discussion

In the following sections, the results of the thermal modeling are first discussed. The results of the physical tests are then discussed in their relation to the predicted results from the thermal modeling. Finally, the sources of error in these tests are discussed.

5.1 Thermal Modeling

The results of the thermal modeling discussed in Section 4.1 can be interpreted to follow what one might expect based on heat-transfer theory.

First, in the discussion of heating rate in Section 4.1.2, the generally strong positive correlation between heating rate and difference in sample and wall temperatures follows apparent logic. In any transient system problem, the system can never react perfectly in sync with a system input. Thus, it is intuitive that as the system of the samples would lag farther behind.

Also discussed in Section 4.1.2 is the integration area of the melt-plateau curve. In the results of these simulations, seen in Figure 29, no strong trend line is seen between heating rate and the integrated area, but instead can be closely represented by the equation $H_f = 0.2983\ A$. Since all of these simulations at various heating rates included the same value of heat of fusion, it is intuitive that these integrals would all be very close to the same value. Assuming that the temporal resolution of the data collection is high enough, the same spike in the dT curve should appear at any heating rate. Given the temporal resolution of this apparatus of up to 100 samples per second, it is predicted that given the mass ratio and heat of fusion outlined in the simulation set-up, any of the

simulated heating rates should be visible in practice. It was hypothesized that the variation around that scaling factor of +/- 7.3% was due to small variations in the shape of the melt-plateau curve due to the temporal resolution of the simulations. It was then shown that at a higher temporal resolution, the melt-plateau curves were of a more uniform shape with much more uniform areas, yielding a variation of only +/- 0.9%.

With regards to the correlations derived in Section 4.1.3, it can be seen that these correlations also follow theoretical logic. First, difference between the "standardized" heating of the samples, with a molybdenum shell thickness and mass of zero, and the heating of the samples was found to decrease exponentially with increasing sample to sample-cup mass ratios. As the sample to sample-cup mass ratio approaches infinity, the sample's behavior would approach the behavior of the standardized sample. On the other hand, as the sample to sample-cup mass-ratio approaches zero, the sample/sample-cup thermal system will be dominated by the sample-cup, and thus will behave similarly to a sample of pure molybdenum.

Similar theory can be applied in the examination of the maximum temperature difference between samples during phase change. In these data, a power-function correlation was noted between sample to sample-cup mass ratio and maximum temperature difference between samples during phase change. As was previously stated, a sample/sample-cup thermal system would behave more like a pure sample with a very high sample to sample-cup mass ratio and more like pure molybdenum at a very low sample to sample-cup mass ratio. Thus, logic is followed as very small

maximum temperature differences between samples are recorded in simulations with very low sample to sample-cup mass ratios. In these simulations, the thermal system is dominated by the molybdenum, which undergoes no phase transformation at 1600^{o}C, and so no melt plateau is detectable.

5.2 Physical Testing

The basic functionality of the sighting tube and wheel mechanism can be inferred from the results of Test I, outlined in Section 4.2.1. As can be seen in Figure 36, four clear individual readings can be seen. It is hypothesized that radiation entering the pyrometer through the four sighting holes are represented by these four readings, as the spacing of the samples is equal to that of the hand-controlled spinning of the sighting wheel. Moreover, it can be seen again in Figure 36, that one peak signal is significantly higher than the other three samples. Due to the testing of the apparatus on an incandescent bulb, it is hypothesized that this sight-tube was aimed directly at the high-temperature filament, while the other three sight tubes were receiving radiation from the area directly around the filament.

In Test II, high temperature differential thermal analysis was attempted to be performed using type C thermocouples for sample measurement and pyrometry for crusceptode temperature measurement. In this test, the difference between the two sample temperatures was examined as a function of reactor temperature. A heating rate of

between 1^{o}C/sec and 2^{o}C/sec was used in this test, theoretical simulations of both of which were calculated in theoretical modeling (see Section 5.1).

The actual recorded data were found to be significantly different than the predicted differences in sample temperature. For example, the actual average recorded difference in temperature between samples during the heating process was 16.588^{o}C, while the theoretical difference calculated in the Icepak simulation was 0.452^{o}C. Similarly, the predicted maximum temperature difference due to the melt plateau was predicted to be 0.41^{o}C based on a sample to sample-cup mass ratio of 2:1. These significant discrepancies are discussed below.

5.3 Sources of Error

After examining the data presented in the previous sections, it is hypothesized that the majority of the discrepancy between theoretical simulated and physical results is on account of error in the physical testing data.

First, some simplifying assumptions were made in the setting-up of the simulations in ANSYS Icepak. First, the geometry of the crusceptode/sample system was simplified. Conduction, other than the very minimal conduction in the argon inside the reaction, was not considered, as it was assumed that radiation would dominate at such high temperatures. This assumption was made based on the fact that heat from radiation, $q_{rad,}$ can be defined as:

$$q_{rad} = \varepsilon \sigma T^4 A$$

Equation 4: Heat transfer due to radiation, with ε = sample emissivity, σ = 5.678 x 10^8 W/m^2K^4 (the Stefan-Boltzmann Constant), T = temperature (K), and A = sample surface area (m^2).

Heat transfer due to conduction can be defined as:

$$q_{cond} = m C_p dT$$

Equation 5: Heat transfer due to conduction with m = sample mass (kg), C_p = sample specific heat (J/kgK), and dT = sample temperature change (K).

Thus, with radiative heat transfer being a function of T^4, this type of heat transfer would dominate at very high temperatures. Still, the effect of heat transfer due to conduction would be non-zero, and thus this is not a perfect assumption.

Nonetheless, it is hypothesized that the theoretical thermal modeling presented above are accurate and that a significant percentage of deviation and error can be explained on account of the physical test set-up and procedure. Two significant sources of error have been hypothesized below.

First, the method of heating by induction was not considered in the thermal modeling simulations. Due to the nature of inductive heating, it is hypothesized that coupling between the inductive field and the thermocouples was occurring during the test. Evidence of this can be seen by examining experimental data. For example, a

significant drop in temperature can be observed when the Lepel is powered off, as seen in Figure 38.

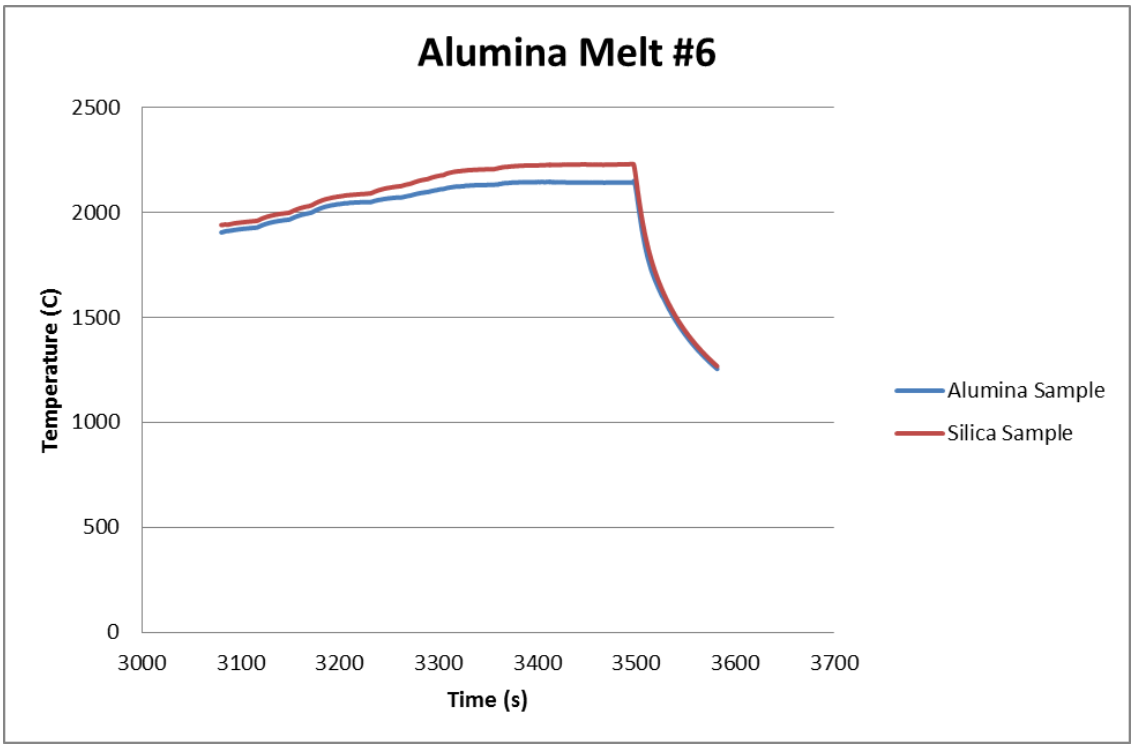

Figure 38: Alumina and silica sample temperatures as a function of time from Test II, melt #6. The sharp drop occurs when Lepel power is turned off.

In the above figure, the temperature difference between the two samples can be seen to drop significantly as the Lepel is powered off. This is a problem which was encountered in a previous test (results not presented in this report), and a solution was attempted. In the aforementioned test, significant coupling was detected in the data. To counteract this, zirconia paste was painted onto the thermocouple wire, at any point where the wire was exposed. It was hoped that this paste would act as an insulator from

the inductive field, and that the thermocouple data would thus not be affected by the field in subsequent thermocouple tests.

Nonetheless, it is hypothesized that despite these attempts at counter-action, the thermocouples were still being affected by the inductive field at an unequal rate. It is possible that this unequal scaling of the values was responsible for the significantly larger temperature difference during the melt plateau than was predicted in the thermal modeling. According to the theoretical model, a temperature difference of only 0.41^{o}C should have been measured during the plateau, due to the relatively low sample to sample-cup ratio of approximately 2:1. Therefore, it is not impossible that the temperature difference and apparent plateau observed was entirely coincidental in its occurring close to the melting point of alumina. This temperature range is fairly close to the upper range in temperature of a type C thermocouple, at 2320^{o}C. It is possible that in the temperature range over 2000^{o}C, one of the thermocouples simple started to fail.

A significant amount of uncertainty can also be derived from the experimental apparatus set-up. The mounting of the thermocouples proved to be extremely difficult. It was found to be nearly impossible to insert the thermocouples, which were lowered through the ports in the top cap of the reactor, without knocking the sample-cups over or otherwise spilling the samples, due to the very limited view of the inner reactor during this process. It was necessary to look in through the gas inlets in the reactor caps, through which one had no depth perception and was thus significantly limited in the ability to accurately maneuver the thermocouple lead. Thus, it is distinctly possible

that the thermocouple heads were placed in contact with the sample cups or at different sample depths. This would lead to significant skewing in the results.

With this in mind, while it was hoped that this test would serve as a calibration and confirmation of theoretical results, it has served more as a reaffirmation of why thermocouples would not make an appropriate temperature measurement apparatus in an induction heated furnace attempting to perform DTA.

6 Conclusions

The conclusions drawn from the results and discussions of this report are presented as follows:

6.1 Thermal Modeling

- The temperature difference between the molybdenum crusceptode and an alumina or silica sample grows exponentialy with reactor temperature and can be calculated as a function of reactor temperature, *T*, and heating rate, *HR*, using:

$$dT_{alumina} = A\, e^{b*T}$$

$$A = 1.5381\ HR^{0.5468} \qquad b = (-8E\text{-}05)\ HR + 0.0016$$

$$dT_{silica} = C\, e^{d*T}$$

$$C = 1.4975\ HR^{0.6889} \qquad d = -0.0001\ HR + 0.0018$$

- The thermal response of a sample/sample-cup system in the reactor was determined to deviate exponentially from a theoretical system in which 100% of the mass was composed of the sample. This deviation can be described using a difference coefficient, *Y*, as a function of sample to sample-cup mass ratio, *MR*, where *Y* decreases as a power function with,

$$Y_{silica} = 8.1633\ MR^{-0.861}$$

$$Y_{alumina} = 6.3458\ MR^{-1.141}$$

- The maximum temperature difference, dT_{max}, between a silica and alumina sample during a melt plateau can be described as an increasing power function of sample to sample-cup mass ratio, *MR*, using

$$dT_{max} = 0.0438\ MR^{2.4073}$$

- A constant correlation was observed between heat of fusion, H_f, and integrated area under the scaled melt-plateau, *A*, curve as a function of heating rate where

$$H_f = 0.2983\ A$$

Thus, the measurement of this area would be recommended as a way to experimentally determine the heat of fusion of an unknown substance.

6.2 Physical Testing

- It can be inferred from initial data from Test I that radiation is appropriately limited to the view area of the sight tube and sight-wheel. Furthermore, it can be observed that radiation is not passed through the sight when the sight-wheel is not over a hole.
- Due to coupling effects, temperature limitations, and extreme difficult in apparatus set-up, it is recommended that thermocouples are not used in the future in the application of high temperature differential thermal analysis.

7 Future Work

As with all research, despite the scope of this project, there inevitably exists more work to be done in the future. Some of this work may be undertaken by this author in the months following the defense of this thesis, while some may be left for future researchers.

First, as of this writing, the UHTIR has yet to be tested with the apparatus designed and assembled for this thesis. This test will likely be performed in April or May of 2013. Results from this test may be included in an addendum to the final copy of this Thesis.

After having performed many hours of testing using the ultra-high temperature induction furnace, there are several areas of improvement which could be recommended. First, preparation of an experiment using this furnace is extremely time-consuming and often difficult. Though significant improvements have been made from the previous design iteration, including improvements in experimental repeatability and safety due to the stand, increased reactor access due to the additional cap and additional ports, the experimental set-up procedure remains complex and problems with repeatability have still been observed.

The most significant improvements could occur in the inner-reactor set-up. One problem which is particularly applicable to this Thesis is the variability of the placement of the crusceptode in the reactor. In set-up, the crusceptode is stacked atop a

series of ceramic pedestals. As of April 2013, a simple visual approximation is used to center these heat pedestals. A great deal of uncertainty is manifested from the stacking of error in this visual centering of these pedestals. Due to the necessity for extreme precision with regards to the location of the crusceptode on the horizontal plane for successful sighting from the pyrometer, it is extremely problematic to have error in this domain.

Thus, it is recommended to establish a more accurate and repeatable system for centering the inner reactor heat shields and pedestals. One possible solution for this might be to develop a system of cylindrical spacers which could be placed in the bottom of the reactor. These spacers would fit between the outer quartz tube and each of the successive heat shields, forcing them into the correct position and not allowing for movement inside the reactor. Both ease of experimental set-up and experimental repeatability would be improved greatly with this type of design.

Next, there are certain improvements that could be made to the DTA apparatus design described in this report. First, the sighting tube currently in use has been manufactured via 3D printer. While this is an appropriate and useful tool for rapid prototyping, a higher level of accuracy would be required to be able to use a purely 3D printer part. Moreover, concern has been raised over the fact that the material, acrylonitrile butadiene styrene (ABS) plastic. ABS plastic features a fairly low melting temperature at 103^{o}C temperature. Based on thermal modeling and experimental data from the undergraduate report, Design and Construction of an Induction Heated Furnace for Molten

Oxide Electrolysis of Rare Earth Elements, it is unlikely that this material would melt in practice [31]. Nevertheless, the apparatus has not been tested at high temperatures mounted to the reactor cap; therefore, it is possible that the melting of the sight could be caused by a high-temperature experiment due to intense radiation coming from the center of the reactor.

Thus, it is recommended that the sight and drive-train apparatus be constructed from a more robust material, particularly one with a higher melting temperature. Since the sight is essentially a cylinder with very narrow drilled out holes, simple machining of this part would likely be possible out of aluminum or another metal. Creating a mold and casting the part would also be an option if many parts were desired.

Another recommendation for future work would be the improvement of the molybdenum sample cup manufacturing process. As of April, 2013, molybdenum sample cups are manufactured by punching holes in molybdenum foil using a standard paper hole-punch and the tiny discs are then punched by hand using a custom stamp. A stamp press which could both press the foil into shape and then cut the cup from the strip of foil would be a useful tool and an improvement in repeatability, as the cups would be more likely to be of a similar size and mass.

Also regarding the sample cups, it is recommended to pre-heat the sample cups before an experimental run. Heating the molybdenum to close to its melting point would increase its ductility. If heated in a mold, the molybdenum would conform to the shape

of the mold, thus relieving the stress of the material and making the sample cups much less likely to crack or fracture. This is especially important to note due to molybdenum's inherently brittle nature.

Next, it would also be worthwhile to develop an integrated system of real-time data analysis using LabVIEW. Currently, data from the pyrometer are available via USB or serial connection and can be stored as raw emissive power or scaled temperature in a standard comma separated value file. It is recommended to develop a VI or sub-VI in LabVIEW, which could be embedded in the main reactor control VI, which could split the data from the four sample cups being viewed and plot the 4 data streams in real time. This would be helpful in viewing short spikes in temperature difference between samples, both during experimental procedure and in post-experimental data analysis.

Finally, there are a number of tests which can be performed both to test the functionality of the apparatus and to perform real research on rare earth materials. As was mentioned at the beginning of this section, a true calibration test will be undertaken to determine the feasibility of the DTA apparatus, which may be included as an addendum to this report. The ultimate goal of this project and this report is to provide an apparatus which can be used for research into material properties of rare earth elements. It is the hope of this author that at the completion of this project and with the aid of this report, this research will be able to be undertaken.

8 References

[1] R. Bud, Instruments of Science: An Historical Encyclopedia, London, 1998.

[2] W. Boettinger, DTA and Heat-Flux DSC Measurements of Alloy Melting and Freezing, Washington, DC: National Instruments of Standards and Technology, 2006.

[3] M. E. Brown, Introduction to Thermal Analysis: Techniques and Applications, 2nd Edition, Dordecht: Kluwer Academic Publishers, 2001.

[4] G. Haxel, "Rare earth elements critical resources for high technology," *United States Geological Survey,* p. 87, 2006.

[5] Babbage, "The Difference Engine: More Precious than Gold," *The Economist,* 2010.

[6] "Rare Earths: Diggin' In," *The Economist,* 2010.

[7] T. C. Andrews, J. Carter, N. Eckman and B. Nakanishi, "Design and Construction of an Induction Heated Furnace for Molten Oxide Electrolysis of Rare Earth Elements," Tufts University, Medford, 2012.

[8] P. J. Sanders, "Characterizing the performance of an induction-heated molten oxide reactor used for the electrowinning of iron," Tufts University, Medford, 2012.

[9] D. R. Sadoway, "New opportunities for metals extraction and waste treatment by electrochemical processing in molten salts," *Journal of Materials Research,* pp. 487-492, 1995.

[10] E. Ramsden, "Temperature Measurement," *Sensors,* 2010.

[11] M. J. Vold, "Differential Thermal Analysis," *Journal of Research of the National Bureau of Standards,* pp. 636-688, 1949.

[12] H. E. Kissinger, "Variation of Peak Temperature With Heating Rate in Differential Thermal Analysis," *Journal of Research of the National Bureau of Standards,* pp. 217-220, 1956.

[13] A. Sembira, "High temperature calibration of DTA and DSC apparatus using encapsulated samples," *Thermochimica Acta,* pp. 113-124, 1996.

[14] R. Pallàs-Areny, Sensors and Signal Conditioning (2nd Edition), New York: 339, 2001.

[15] S. L. BOERSMA, "A Theory of Differential Thermal Analysis and New Methods of Measurement and Interpretation," *Journal of American Cermaic Society,* pp. 281-284, 2006.

[16] J. L. Caslavsky, "Melting behaviour and metastability of yttrium aluminium garnet (YAG) and YAlO3 determined by optical differential thermal analysis," *Journal of Materials Science,* pp. 1709-1718, 1980.

[17] C. Cao, "Liquid phase separation in undercooled Co–Cu alloys processed by electromagnetic levitation and differential thermal analysis," *Journal of Alloys and Compounds,* pp. 113-117, 2001.

[18] A. Bergman, Fundamentals of Heat and Mass Transfer, Hoboken: John Wiley and Sons, Inc., 2011.

[19] R. Siegel, Thermal Radiation Heat Transfer, 4th Edition, New York, 2002, p. 132.

[20] R. 1. C. Defoe C. Ginnings, "Enthalpy, Specific Heat, and Entropy of Aluminum Oxide," *Journal of Research of the National Bureau of Standards* , pp. 593-600, 1947.

[21] K. Davis, "Material Review: Alumina (Al2O3)," *School of Doctoral Studies (European Union) Journal,* pp. 109-114, 2010.

[22] E. C. a. D. Shah, "Measurement of Diffusivities of Helium and Argon in Silicalite," *Journal for the Basic Principles of Diffusion Theory, Experiment and Application,* pp. 1-2, 2005.

[23] R. T. J. E. W. Lemmon, "Viscosity and Thermal Conductivity Equations for Nitrogen, Oxygen, Argon, and Air," *International Journal of Thermophysics,* pp. 21-69, 2004.

[24] "The Specific Heat of Molybdenum From 250°C to -40°C," *The American Physical Society,* 1928.

[25] R. D. Allen, "Spectral Emissivity, Total Emissivity, and Thermal Conductivity of Molybdenum, Tantalum, and Tungsten above 2300°K," *Journal of Applied Physics,* pp. 1382-1387, 1960.

[26] e. a. J. Kestin, "Viscosity of Noble Gases in the Temperature Range 25-700C," *Journal of Chemical Physics,* pp. 4119-4124, 1971.

[27] J. Pattison, "Total emissivity of some refractory materials above 900C," *Journal of the British Ceramic Society,* pp. 698-705, 1955.

[28] e. a. A. H. Sully, "Some measurements of the total emissivity of metals and pure refractory oxides and the variation of emissivity with temperature," *Journal of Applied Physics,* pp. 98-101, 1952.

[29] E. P. Mikol, "The Thermal Conductivity of Molybdenum Over the Temperature Range 1000-2100F," *Metallurgy and Ceramics,* 1982.

[30] N. Kallay, Interfacial Dynamics, New York: Eastern Hemisphere, 2000.

[31] T. C. Andrews, J. Carter, N. Eckman and B. Nakanishi, "Design and Construction of an Induction Heated Furnace for Molten Oxide Electrolysis of Rare Earth Elements," Tufts University, Medford, 2012.

9 Appendix

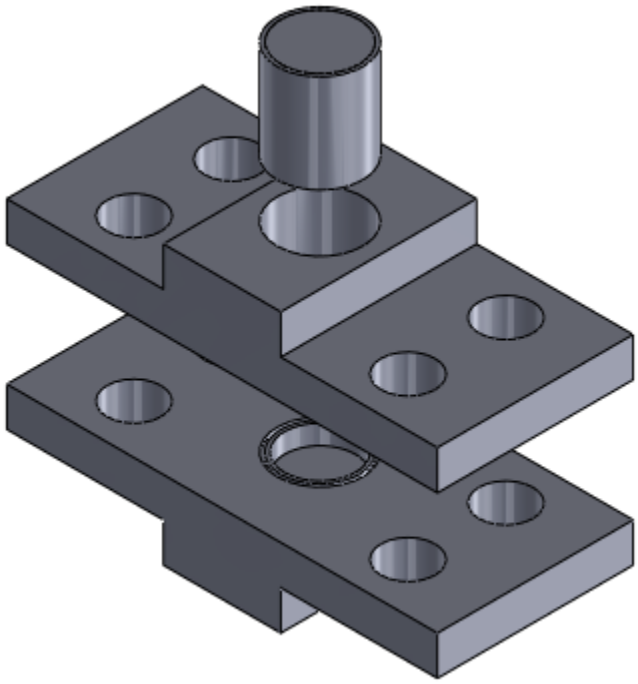

Appendix Figure 1: The design for a stamp press for the press of molybdenum foil sample-cups. The male and female parts were the only parts manufactured.

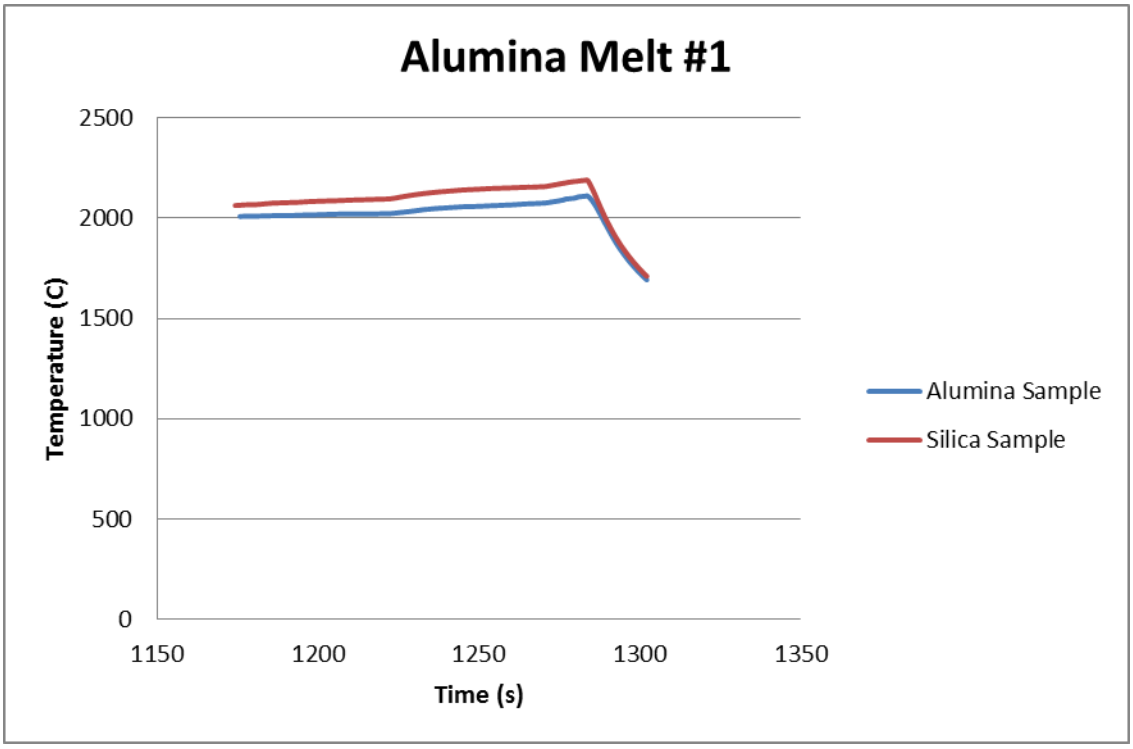

Appendix Figure 2: Thermocouple data from heating and cooling #1 through the melt plateau of alumina during Test II.

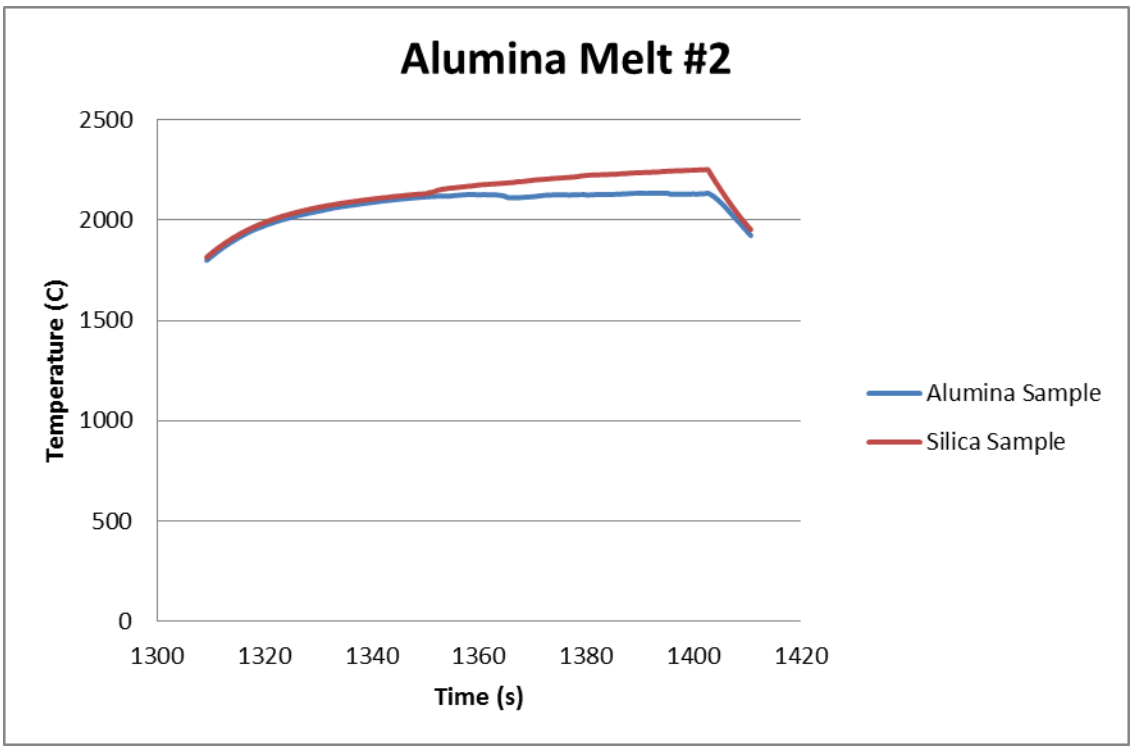

Appendix Figure 3: Thermocouple data from heating and cooling #2 through the melt plateau of alumina during Test II.

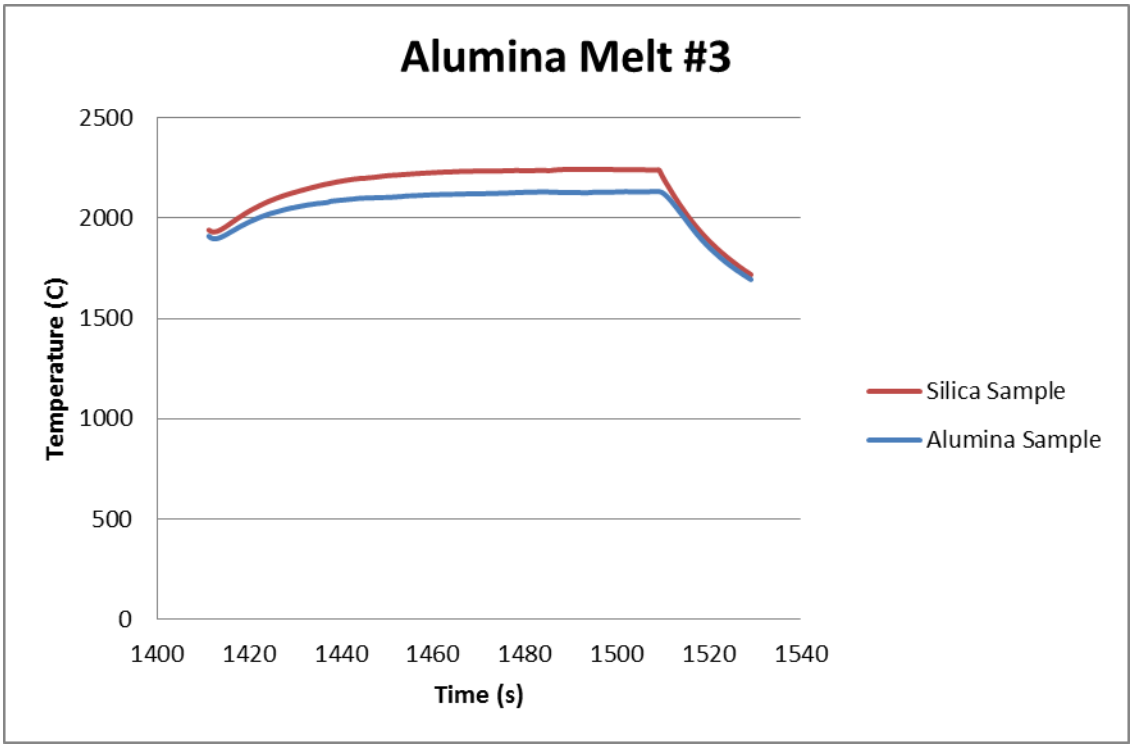

Appendix Figure 4: Thermocouple data from heating and cooling #3 through the melt plateau of alumina during Test II.

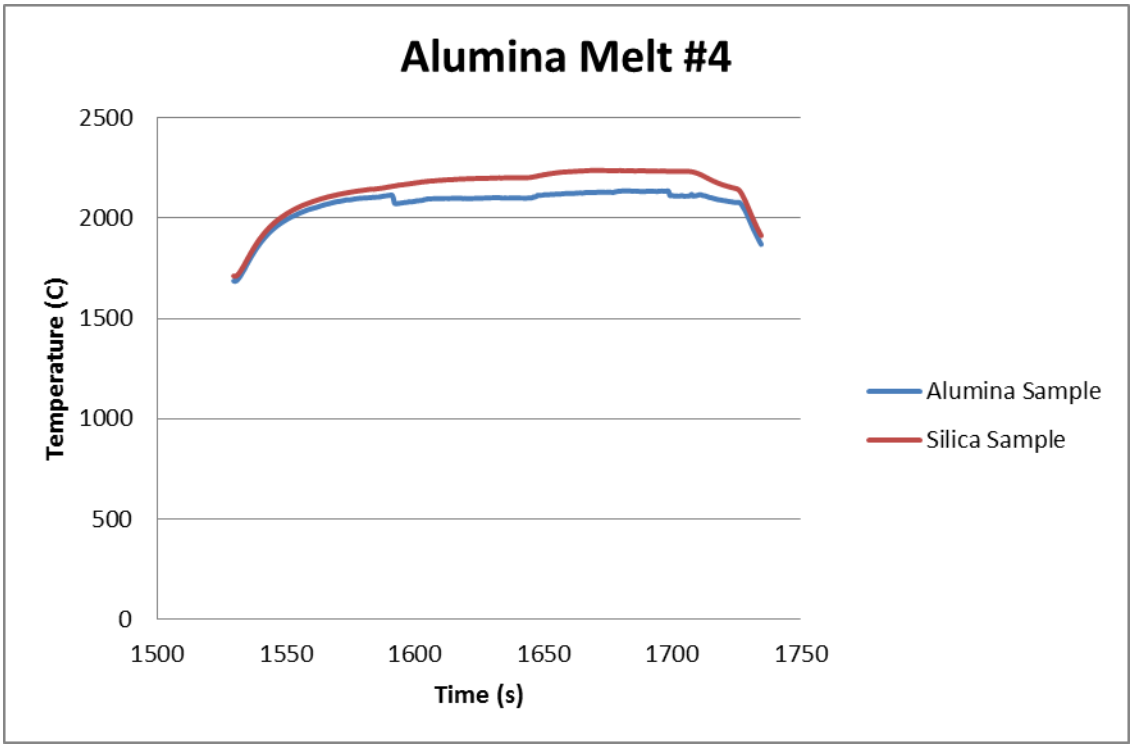

Appendix Figure 5: Thermocouple data from heating and cooling #4 through the melt plateau of alumina during Test II.

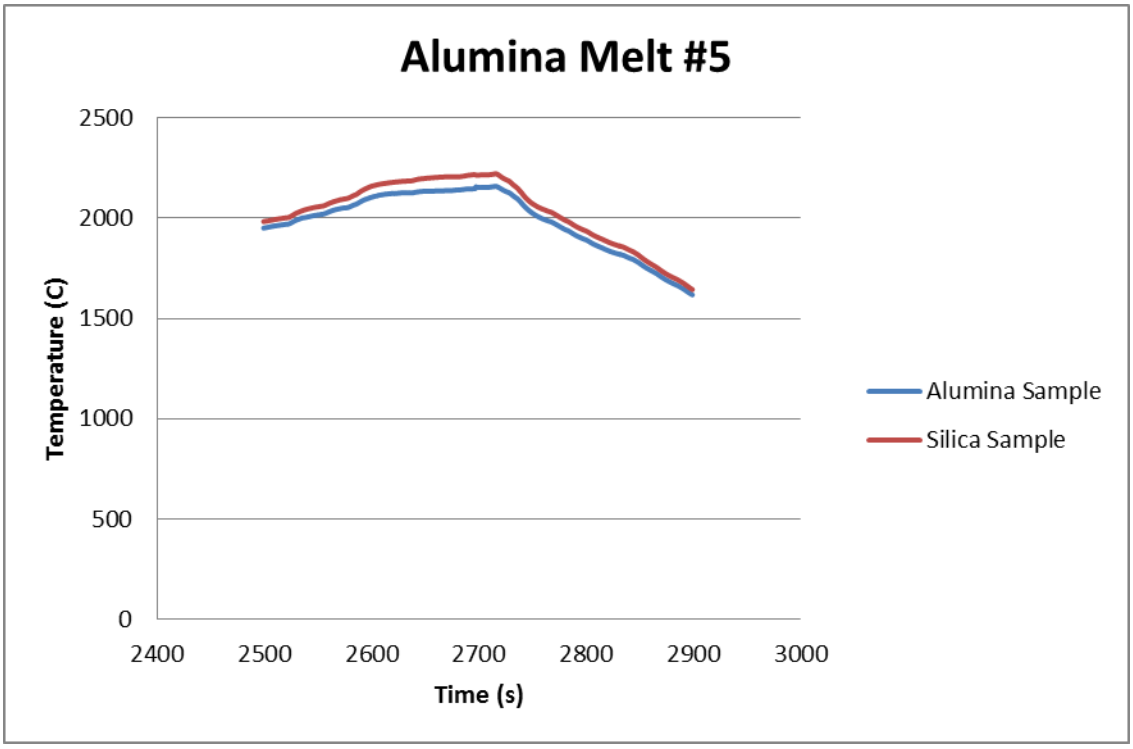

Appendix Figure 6: Thermocouple data from heating and cooling #5 through the melt plateau of alumina during Test II.

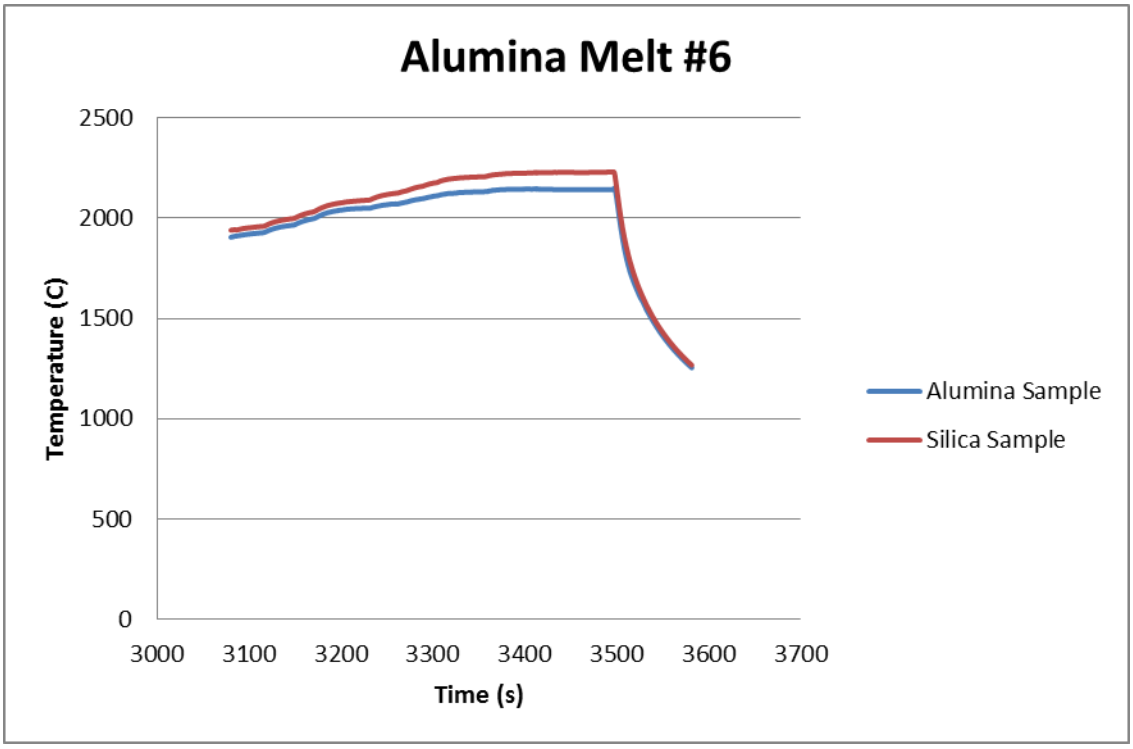

Appendix Figure 7: Thermocouple data from heating and cooling #6 through the melt plateau of alumina during Test II.

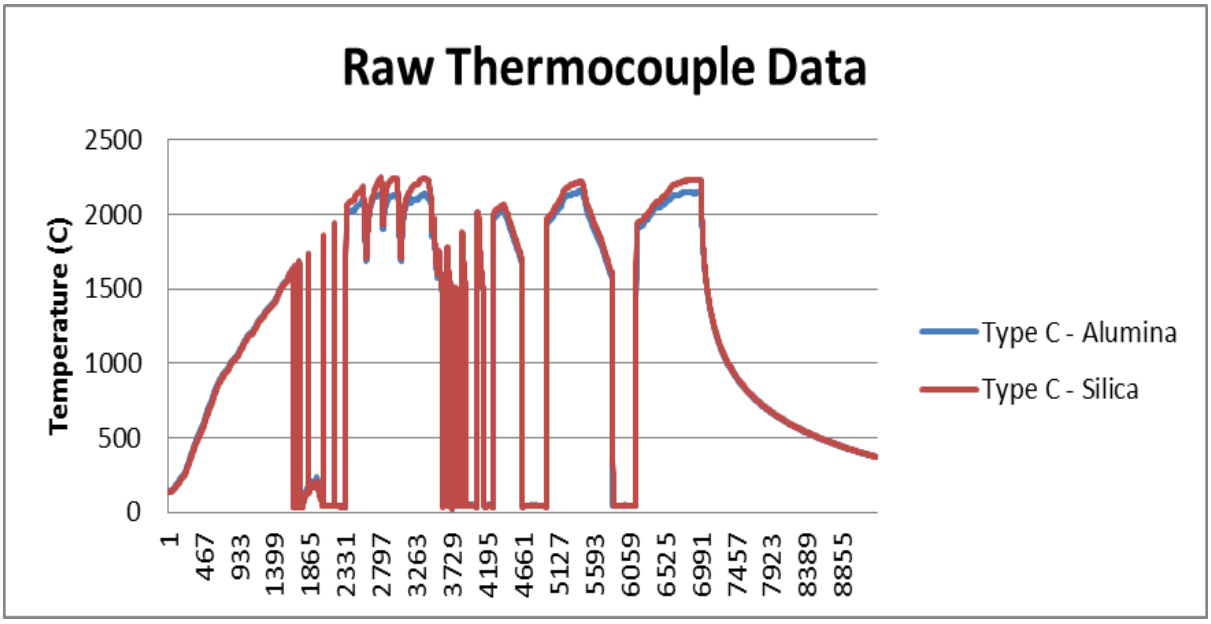

Figure %%: All raw thermocouple data from Test II. The ranges where the thermocouples failed can be clearly seen as the sharp drops in signals.